UCLA
UCLA Electronic Theses and Dissertations

Title
Development of Capacitive Tactile Sensors for Surgical Systems

Permalink
https://escholarship.org/uc/item/5kb1z84z

Author
Dai, Yuan

Publication Date
2015

Peer reviewed|Thesis/dissertation

eScholarship.org Powered by the California Digital Library
University of California

UNIVERSITY OF CALIFORNIA

Los Angeles

Development of Capacitive Tactile Sensors for Surgical Systems

A dissertation submitted in partial satisfaction

of the requirements for the degree Master of Science

in Electrical Engineering

by

Yuan Dai

2016

© Copyright by

Yuan Dai

2016

ABSTRACT OF THE THESIS

Development of Capacitive Tactile Sensors for Surgical Systems

by

Yuan Dai

Master of Science in Electrical Engineering

University of California, Los Angeles, 2016

Professor Robert N. Candler, Chair

Minimally invasive surgery (MIS) has gained popularity over traditional open surgery due to its advantages of decreased incision size and pain to the patient, lower risk of infection, and shorter recovery time. Recent developments in robotic surgical systems have shown promise to further advance MIS by offering the surgeons with increased manipulability and dexterity along with 3D vision.

However, one major disadvantage associated with robotic surgery is the absence of tactile feedback, which is critical in tool-tissue interaction. This paper provides an overview and information useful for approaching a novel tactile feedback sensor system.

We aim to construct highly sensitive micro-scale tri-axial capacitive-based differential force sensors that will be integrated at the tips of surgical tools used in robotic surgery. To date, three capacitive sensor models have been proposed. Comb drive model, joystick model and single-sided capacitive sensor model. The first two models were initially created by COMSOL, with optimized geometry parameters. We demonstrate that all three models can satisfy the sensitivity and resolution requirement after being connected with a readout circuit. The fabrication process is proposed and short-loop experiments have been conducted.

The integration of read-out circuits with the capacitive sensor is designed on a flexible printed circuit board, which will be first connected to the computer with LabVIEW based controller to convert the analog signal to digital capacitor signal, and the force information as well as the real-time sensitivity, resolution values can be obtained. After the functionality of the sensor is proven to be valid, the proposed tactile sensor system needs to integrate into current Haptic Feedback System. Both the microcontroller and the software need to be modified to function with the proposed sensor and the actuators.

The thesis of Yuan Dai is approved.

Pei-Yu Chiou

Warren Grundfest

Robert N. Candler, Committee Chair

University of California, Los Angeles

2016

TABLE OF CONTENTS

Chapter 1: INTRODUCTION 1
1.1. Minimally Invasive Surgery 1
1.1.1. Laparoscopic Surgery 1
1.1.2. Robotic Surgery 2
1.2. Today's Problems/ Challenges 3
1.3. The Scope of this Work 4
1.4. Organization of this Thesis 4
References 5
Chapter 2: TACTILE SENSOR TECHNOLOGIES 6
2.1. Functional and Technical Requirement 6
2.2. Sensor Types and Basic Working Principles 8
2.2.1. Piezoresistive sensors 8
2.2.2. Capacitive sensors 10
2.2.3. Piezoeleenctric sensors 11
2.2.4. Optical sensors 12
2.2.5. Magnetic sensors 13
2.3. Comparison of Different Sensor Types 13
References 15
Chapter 3: CAPACITIVE SENSOR DESIGN 18
3.1. Literature Review and Design Insights of Capacitive Sensor 18
3.1.1. Review of 3-axis capacitive sensors 18
3.1.2. Design insights 21
3.2. Comb Drive Model 23
3.2.1. Schematic of comb drive design 23
3.2.2. Sensitivity calculation 23
3.2.3. Results and discussion 25
3.3. Joystick Model 26
3.3.1. Schematic of joystick design 26
3.3.2. Sensitivity calculation 27
3.3.3. Optimal design parameters 31
3.3.4. Fabrication process 32
3.4. Single-sided Sensor Model 36
3.4.1. Schematic of single-sided sensor design 36
3.4.2. Sensitivity calculation 37
3.4.3. Fabrication process 45
3. 5 Discussion 46
References 47
Chapter 4: INTEGRATION 48
4.1. Integration with Operating Grasper 48
4.2. Capacitance-to-Digital Converter AD7746 49
4.2.1. Comparison between different CDCs 49

4.2.2. Pin layout for AD7746 ... 50
4.2.3. Data acquisition from AD7746 ... 52
4.3. Flexible PCB Design ... 56
4.3.1. First generation PCB design for joystick model ... 56
4.3.2. Improved PCB design for single-sided sensor model ... 59
4.4. Functionality Testing ... 62
4.5. Integration with Haptic Feedback System ... 68
4.6. Results and Discussion ... 70
References ... 73
Chapter 5: SUMMARY ... 74

LIST OF FIGURES

Figure 1 (a) Laparoscopic procedure and (b) open surgery by Wottawa [4] 1
Figure 2 Demonstration of roll, yaw, and pitch 2
Figure 3 The da Vinci surgical system by Wottawa [4] 2
Figure 4 A parallel plate capacitive sensor 10
Figure 5 Schematic of a shear stress sensing element (a) without applied forces, (b) with a normal force, (c) with a shear force (d) detailed design of the sensing element by Cheng *et al*[1] 18
Figure 6 (a) Design of the capacitive sensor, with top and bottom electrodes embedded in three layers of polymeric packaging (b) the schematic of the sensing element: the finger shape electrodes form four unit capacitors C_1–C_4, which can support 3-axis sensing by Dobrzyns *et al* [2]. 19
Figure 7 (a) Cross section view of the sensing cell (b) Each unit cell consists of an X-cell and a Y-cell which measure normal stress and shear in x- and y-directions represented by the arrows, respectively (c) sensing schematics: capacitances C_1 and C_2 belong to the X-cells C_3 and C_4 belong to the Y-cell. (i) A sensing cell under only normal force and (ii) with both shear and normal force [3]. 20
Figure 8 (a) Schematic of the sensing structure (b) configuration of the bottom electrode: the triangular shaped electrodes are used to measure F_z, M_x and M_y, the comb structures are used to measure F_x, F_y, and M_z. (c) normal force sensing: capacitance change because of the decreased gap distance (d) shear force sensing: differential change in capacitance between electrodes C_a and C_b with respect to the top electrode because of the silicon pillars bending by Brookhu *et al* [4] 21
Figure 9 Schematic drawing of comb drive model for both compression sensing and shear sensing 23
Figure 10 Read-out circuit for a differential capacitive sensor 24
Figure 11 COMSOL simulation capacitance vs force, leading to the sensitivity be 3 fF/N 26
Figure 12 Working principle of joystick model. The center plate can detect normal force while the surrounded four parts of electrodes are capable of sensing shear force. 27
Figure 13 Schematic drawing for one trapezoid in the capacitive sensor design 27
Figure 14 Sensitivity dc/dx with respect to different angle (in degree) 28
Figure 15 Geometry of the top layer of the joystick model 29
Figure 16 Change of capacitance with compression force 0-10N for (a) different materials, (b) different electrode dimensions with PDMS as the dielectric. 32
Figure 17 Change of capacitance with shear force 0-10N for (a) different materials, (b) different electrode dimensions with PDMS as the dielectric. 32
Figure 18 Fabrication process (a) PECVD SiO2 (b) Au deposition of bottom layer (c) PDMS coating (d) photolithography to define top layer (e) Au deposition of top Au layer (f) strip plating mold (g) substrate removal (h) backend process to integrate to FPCB 34
Figure 19 Schematic for single-sided capacitive sensor 37
Figure 20 Illustration of how capacitance change with normal force 37

Figure 21 Comparison between estimated value and the accurate value from complete analytical mode for calculation of normal force given normal capacitance, and calculation of normal capacitance given normal force.......... 38
Figure 22 illustration of how capacitance change with shear force 40
Figure 23 Size information for each fabricated plate.......... 40
Figure 24 Assumption that $M \approx 1$ is valid up to 100N from the left figure. Capacitance calculated with and without the assumption is compared shown on the right figure.. 43
Figure 25 Calculation of shear force given shear capacitance.......... 43
Figure 26 Square-root estimation, linear estimation, and the calculated shear force given shear capacitance.......... 44
Figure 27 Fabrication process (a) silicon substrate (b) thermal oxidation 850nm (c) evaporation and liftoff (d) selective removal of backside silicon dioxide (e) 300um deep FDRIE (f) spin on and cure PDMS (g) evaporation and liftoff (h) cleave sample and release final device . 46
Figure 28 Schematic of integration the capacitive sensor to the surgical grasper.......... 48
Figure 29 AD7746 pin layout 50
Figure 30 Application diagram for a differential capacitive sensor for chip AD7746 [2].......... 51
Figure 31 Illustration of wire connection for single-sided sensor with AD7746.......... 52
Figure 32 (a) Footprint of AD7746 (b) schematic of AD7746 (c) package of AD7746.......... 56
Figure 33 Schematic for joystick model integrated circuit 57
Figure 34 Working principle of the integrated capacitive sensor 58
Figure 35 Working principle of the integrated voltage controlled capacitor 58
Figure 36 Comparison between capacitive sensor and varactor. 58
Figure 37 Schematic and 3D layout for the PCB design 59
Figure 38 (left)PCB layout for single-sided sensor (right) real object after soldering components 59
Figure 39 A triple 3-to-1 multiplexer ADG793A.......... 60
Figure 40 Schematic for now and after integration plan.......... 61
Figure 41 Screenshot for schematic for the integrated FLEX board.......... 61
Figure 42 Schematic for system level design 62
Figure 43 Screenshot for LabVIEW program user interface for testing AD7746.......... 63
Figure 44 One example setup for the registers.......... 63
Figure 45 Screenshot for getting Hex output capacitance and voltage value diagram. 64
Figure 46 Screenshot for read register diagram.......... 65
Figure 47 Screenshot for capacitance resolution calculation 66
Figure 48 Screenshot for normal force calculation, sensitivity and resolution output schematic 67
Figure 49 Play alarming sound diagram.......... 67
Figure 50 LabVIEW user interface 68
Figure 51 Arduino due board.......... 69
Figure 52 Normal force testing with single-sided capacitive sensor.......... 70
Figure 53 Shear force testing with single-sided capacitive sensor 71

LIST OF TABLES

Table 1 Comparison between traditional open surgery, laparoscopic surgery and robotic surgery 3
Table 2 Sensory specifications of human fingertip 6
Table 3 Design guidelines for tactile sensing systems 8
Table 4 Comparison of the reviewed sensing techniques [3,4] 13
Table 5 Material properties 36
Table 6 Comparison for different CDCs 50
Table 7 Register condition for different situations 55
Table 8 Register configuration for proper setup 55
Table 9 Typical capacitive input noise vs. conversion time 72

LIST OF ACRONYMS

ADC	analog-to-digital converter
AOE	advanced oxide etcher
CDC	capacitance-to-digital converter
AMR	anisotropic magnetoresistive
CPU	central processing unit
FPCB	flexible printed circuit board
FSR	free spectrum range
FTI	flexible tactile imager
GMR	giant magnetoresistive
GPIO	general purpose input/output
HFS	haptic feedback system
IDE	integrated development environment
I2C	inter-integrated circuit
MEMS	microelectromechanical systems
MIS	minimally invasive surgery
MUX	multiplexer
MR	magnetoresistive
OFET	organic field effect transistor
PCB	printed circuit board
PDMS	polydimethylsiloxane
PE	polyethylene
SCL	serial clock line
SDA	serial data line
SPI	serial peripheral interface
TMR	tunneling magnetoresistive
UART	universal asynchronous receiver/ transmitter

Chapter 1: INTRODUCTION

1.1. Minimally Invasive Surgery

Minimally invasive surgery (MIS) is a surgery that is less invasive than traditional open surgery. In open surgery, a surgeon views the field directly from a large incision area and performs surgery with his or her hands or hand-held tools, while in MIS procedures, surgeons look through an endoscope and external monitors into smaller incisions (typically 0.5 cm to 1.5 cm) to accomplish identical tasks [1-3].

1.1.1. Laparoscopic Surgery

Laparoscopic surgery is a minimally invasive surgery that has the surgical area around patient's abdomen. Fig. 1 demonstrates the comparison between a laparoscopic surgery and an open surgery.

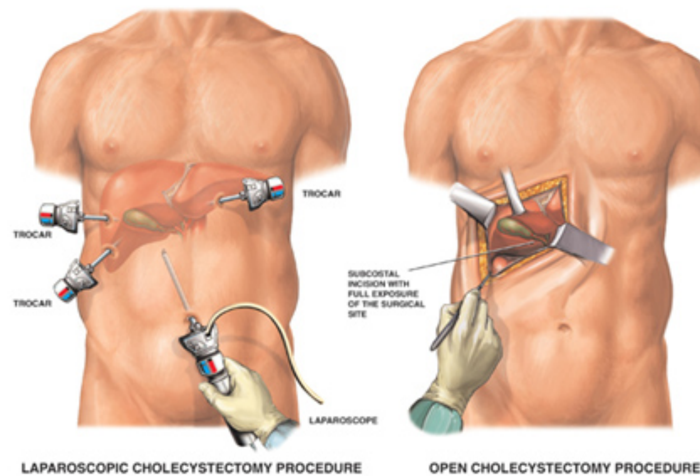

Figure 1 (a) Laparoscopic procedure and (b) open surgery by Wottawa [4]

Despites the advantages associated with laparoscopic surgery, it is missing two degrees of freedom from human wrist motion, i.e., yaw and pitch. As for a human, our wrist has seven degrees of freedom. Besides the commonly known three degrees of freedom in translation, *x, y,*

and z, and one degree of freedom of grasping, we have three degrees of freedom in rotation: pitching, yawing, and rolling. Rolling is the rotation around longitudinal axis (pivoting side to side), pitching is the rotation around the lateral axis (tilting forward and backward), and yawing is the rotation around the vertical axis (swiveling left and right). Fig.2 is an illustration for pitch, yaw, and roll.

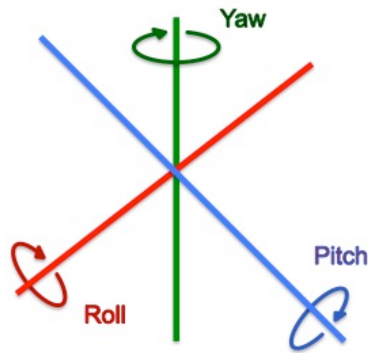

Figure 2 Demonstration of roll, yaw, and pitch

1.1.2. Robotic Surgery

Robotic surgery offers an alternative to conventional laparoscopic surgery where the surgeons directly control surgical instruments. Fig. 3 shows a typical master-slave robot-assisted da Vinci surgical system.

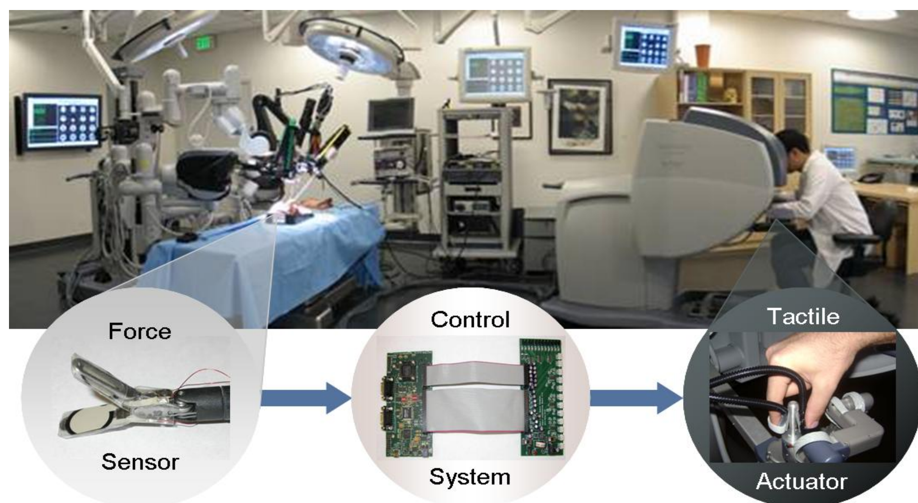

Figure 3 The da Vinci surgical system by Wottawa [4]

Laparoscopic and robotic surgery techniques have gained popularity for minimal scarring, reduced trauma and shorter recovery time compared to the traditional open surgery. Unfortunately, since surgeons performing laparoscopic surgery are not in direct contact with the patient, their lack of tactile feedback has become a big issue. The extensive grasping force causes tissue damage because of lack of tactile feedback.

The advantages and disadvantages of traditional open surgery, laparoscopic surgery and robot-assisted surgery are summarized in Table 1.

Table 1 Comparison between traditional open surgery, laparoscopic surgery and robotic surgery

	Robot-assisted surgery	***Laparoscopic***	***Open surgery***
Pros	• Virtually scar-less • Reduced trauma • Shorter recovery time • Tremor removal • 3-D visualization • Scaled movements	• Minimal scarring • Reduced trauma • Shorter recovery time • Affordable and ubiquitous	• Direct contact with patient • Surgeon familiarity • Availability
Cons	• Longer surgeries • Expensive tooling • Lack of tactile feedback	• Loss of 3D vision • Compromised dexterity • Lack of tactile feedback	• Scar formation • Long recovery periods • Painful

1.2. Today's Problems/ Challenges

Attempts to resolve this complete absence of tactile feedback dilemma for robotic surgery have resulted in the development of haptic feedback design for minimally invasive surgery. Numerous attempts on different modalities and designs of tactile sensors have been made.

However, few attempts have been conducted to make integrated tactile feedback sensor for both normal and shear force with surgical tools. Not to mention none of the methods developed is perfect and all are far from ready to be used in commercial systems.

1.3. The Scope of this Work

A major effort of this thesis is to discuss approaches and strategies for structuring an efficient and effective three-axial tactile feedback system, which provides surgeons with intelligent, computer aided instructions for manipulating surgical tools. After that, the final goal of integration with the current haptic feedback system is also crucial in our project.

We preliminarily focus on the capacitive tactile feedback sensor design, it needs to give us sufficient functionality for initial evaluations of tactile feedback; more research is still required before final goal of integrating sensors into surgical system can be completed.

1.4. Organization of this Thesis

The structure of the thesis is organized as follows:

In Chapter 2, an overview of basic physical principles of sensing technologies, piezoresistive sensors, capacitive sensors, piezoelectric sensors, optical sensors, and magnetic based sensor are provided. This is followed by a discussion of the functional and technical requirements for the three-axial tactile feedback sensor.

The design and analysis of proposed models is presented in Chapter 3. We start with a review of state-of-the-art capacitive sensor design. Based on the previous discussion, three geometries, comb drive model, joystick model, and single-sided capacitive sensor model are proposed. Various ways of justification and the reasons for their choice are discussed briefly. Analytical and simulation results are also provided.

This is followed by a discussion about integration of designed capacitive sensor, readout circuit to the surgical tools as well as the current haptic feedback system in Chapter 4. After the analysis is carried out with a LabVIEW program for verification of the functionality of our sensor, the integration with HFS is done by modifying the microcontroller and the programming software.

Chapter 5 contains some conclusions plus future directions of research.

References

[1] " Advanced care in surgical specialties". http://www.camdenclark.org/ChoosingUs/Surgical.aspx

[2] "MIS Surgery". http://www.surgicalpracticesofstx.com/general-surgery/mis-surgery

[3] "Laparoscopic Surgery". http://www.mmssurgery.com/specialty-areas/laparoscopic-surgery.html

[4] Wottawa, C.R., "An Investigation into the Benefits of Tactile Feedback for Laparoscopic, Robotic, and Remote Surgery," Ph.D. dissertation, Univ. of California, Los Angeles, 2013

Chapter 2: TACTILE SENSOR TECHNOLOGIES

A considerable amount of research has been done on tactile sensor design and fabrication during the last decade. There are many candidates for tactile sensing: resistive sensors, capacitive sensors, inductive sensors, piezoelectric sensors, optical sensors, magnetic sensors, ultrasonic sensors, magnetoelectric sensors, and organic field effect transistor (OFET) sensor. A summary of some of the relevant concepts and specifications in sensing are presented in this section.

2.1. Functional and Technical Requirement

The basis for robotic tactile sensing should trace back to human tactile sensing.

Table 2 shows the human fingertip's capability [1], which gives us the criteria for sensor design in the best scenario.

Table 2 Sensory specifications of human fingertip

Parameter	***Value***
Frequency response	0 - 100 Hz
Response range	0 – 100 g/mm^2
Sensitivity	~ 0.2 g/mm^2
Spatial Resolution	1.8 mm

Artificial sensor characteristics include resolution, transfer function, sensitivity, calibration, linearity, hysteresis, accuracy, span or dynamic range, and noise. Listed below are the definitions and classifications for some of the important characteristics for sense of touch [2].

- Transfer function: the relationship between the input physical input signal and the output electrical signal
- Sensitivity: the ratio of the output signal to the input signal, i.e., the slope of the transfer function

- Linearity: the output signal of the sensor is linear increase or decrease with the change of the input signal
- Hysteresis: sensors do not have the same output value when the input signal return to its original value from a different path from previous
- Accuracy: measured as the maximum discrepancy between the actual value and the ideal value
- Span or dynamic range: two definitions can be used in the sensors. One is the range of the input signal and the other is the ratio of the maximum input signal value to the minimum input signal value, for example, 1000: 1
- Noise: can be divided into two categories, inherent noise within the circuit and interference noise picked up from outside of the circuit
- Resolution: the ratio of the noise to the sensitivity of the sensor
- Response time: amount of time passed between the application of a physical input signal and the resulting indication of that change in the output electrical signal

Common sense lead us thinking that the humidity effect would affect the stability of the sensor, temperature variance would affect the sensitivity of the sensor, and susceptibility to electromagnetic interferences would affect the frequency response of the sensor. In short, the environmental factors affect the sensor characteristics to a large extent and must be considered when choose the sensor design.

Following the previous discussion and pioneers hard work, some basic design criteria can be formulated for tactile sensing in a robotic surgery system [1, 3, 4], as addressed in table 3.

Table 3 Design guidelines for tactile sensing systems

Design criteria	***Guideline***
Sensing surface	Compliant and durable
Force direction	Both normal and tangential
Spatial resolution	2 mm
Temporal variation	Both dynamic and static
Minimum force sensitivity	1 gram force (0.01N)
Force range/ Dynamic range	0.01-10 N/ About 1000:1
Linearity	Monotonic, not necessary linear
Frequency response	At least 100 Hz
Time response	1 ms
Stability and repeatability	Good
Robustness	Withstand application defined environment
Hysteresis	Low
Integration and fabrication	Simple, minimal wiring, low power consumption and low cost

2.2. Sensor Types and Basic Working Principles

2.2.1. Piezoresistive sensors

A piezoresistor sensor detects mechanical stress/ strain by a change in resistance of the piezoresistive material itself [5, 6]. As a result, piezoresistive sensor is also called a strain gauge.

The underlying physics of the electrical conductivity σ / resistivity ρ change comes from changing of the effective mass, m^*.

$$\frac{1}{\rho} = \sigma = \frac{qt}{m^*}$$

which is caused by changing of the shape of energy band. In the above expression, q is the elementary charge of an electron and t is the diffusion constant. With *E(k)* being the electron energy of at wavevector k in that band, $\hbar$ being the reduced Planck constant,

$$m^* = \frac{\hbar^2}{d^2E(k)/_{dk^2}}$$

rising from the crystal lattice deformation, as a result of applied strain/ stress. In short, the resistivity of a material depends on the internal atom positions and their motions. Strains change these arrangements and, hence, the resistivity.

Now knowing that the resistivity is sensitive to stress, we can write

$$\rho = \rho_{no\ stress} + \Delta\rho(s, \tau)$$

Where s and τ are the normal and shear tensile stress components, respectively.

Writing the Ohms' Law with respect with electric field ***E*** and current density ***J*** in matrix form:

$$\begin{bmatrix} E_1 \\ E_2 \\ E_3 \end{bmatrix} = \begin{bmatrix} \rho_1 & \rho_6 & \rho_5 \\ \rho_6 & \rho_2 & \rho_4 \\ \rho_5 & \rho_4 & \rho_3 \end{bmatrix} \begin{bmatrix} J_1 \\ J_2 \\ J_3 \end{bmatrix}$$

we have the relationship between the change of resistance $\Delta\rho$ and the applied stress s and strain τ as:

$$\frac{1}{\rho}\begin{bmatrix} \Delta\rho_1 \\ \Delta\rho_2 \\ \Delta\rho_3 \\ \Delta\rho_4 \\ \Delta\rho_5 \\ \Delta\rho_6 \end{bmatrix} = \begin{bmatrix} \pi_{11} & \pi_{12} & \pi_{13} & 0 & 0 & 0 \\ \pi_{12} & \pi_{11} & \pi_{12} & 0 & 0 & 0 \\ \pi_{12} & \pi_{12} & \pi_{11} & 0 & 0 & 0 \\ 0 & 0 & 0 & \pi_{44} & 0 & 0 \\ 0 & 0 & 0 & 0 & \pi_{44} & 0 \\ 0 & 0 & 0 & 0 & 0 & \pi_{44} \end{bmatrix} \begin{bmatrix} s_1 \\ s_2 \\ s_3 \\ \tau_1 \\ \tau_2 \\ \tau_3 \end{bmatrix}$$

where π_{ij} are piezoresitive coefficients in the longitudinal and transverse direction. To identify the directions, three axes termed 1, 2, and 3 are used, analogous to X, Y, and Z of the classical three dimensional orthogonal set of axes. From the above expression, the corresponding stress can be detected with the change of resistance.

Piezoresistive responses are more significant in semiconductor materials like silicon, germanium, than in metal. However, it should be noted that semiconductor piezoresistive sensors are quite sensitive to temperature variations too. Therefore, temperature-compensating networks must be implemented. Two techniques are commonly used. The first is to apply a reference resistor which is subject to the same temperature but not strain, and the difference will be used to account for the strain effect. The second technique is to connect the gauge to a Wheatstone bridge circuits.

2.2.2. Capacitive sensors

The fundamental structure of a capacitive sensor is of two flat parallel plates with area *A* and distance *d* (Fig. 4)

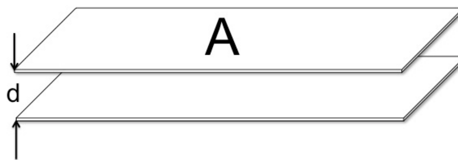

Figure 4 A parallel plate capacitive sensor

When *d* is much smaller than the dimension of the plates, the capacitance equation is valid:

$$C = \frac{\varepsilon_0 \varepsilon_r A}{d}$$

where ε_0 is permittivity of vacuum ($\varepsilon_0 = 8.85 \times 10^{-12} F/m$), and ε_r is the relative permittivity of the dielectric material in between the plates.

This formula is the key to design capacitive sensor, by establishing the relationship between the capacitance and the plate area, the distance and the relative dielectric constant of the material. Varying either the overlap area or the distance will change the capacitance's value, and changing the dielectric material will change the sensitivity of the sensor. It should be noted that the

equation $C = \frac{\varepsilon_0 \varepsilon_r A}{d}$ holds only for parallel capacitor. A change of the geometry will require a modified formula.

Capacitive sensors [7, 8, 9, 10] benefit from low cost, easy fabrication, and high sensitivity. However, complex electronics are needed to measure the capacitance and to derive the relative position.

2.2.3. Piezoelectric sensors

Piezoelectric based sensors [11, 12, 13, 14] can be treated as force sensitive voltage sources. They convert an applied force or stress (accounting the contacting area) into an electrical potential difference, i.e., voltage, which arises from polarization.

The electric displacement D is defined as

$$D \equiv \varepsilon_0 E + P$$

where E is the electric field, P is the polarization density. The polarization density P and the stress is related by the following expression $P = dT$, where d is piezoelectric strain constant, T is stress vector composed of normal stress s and shear stress τ as mentioned in section 2.2.1. Writing the formula in matrix form, we have

$$\begin{bmatrix} D_1 \\ D_2 \\ D_3 \end{bmatrix} = \begin{bmatrix} \varepsilon_{11} & 0 & 0 \\ 0 & \varepsilon_{22} & 0 \\ 0 & 0 & \varepsilon_{33} \end{bmatrix} \begin{bmatrix} E_1 \\ E_2 \\ E_3 \end{bmatrix} + \begin{bmatrix} 0 & 0 & 0 & 0 & d_{15} & 0 \\ 0 & 0 & 0 & d_{24} & 0 & 0 \\ d_{31} & d_{32} & d_{33} & 0 & 0 & 0 \end{bmatrix} \begin{bmatrix} s_1 \\ s_2 \\ s_3 \\ \tau_1 \\ \tau_2 \\ \tau_3 \end{bmatrix}$$

The generated voltage V from piezoelectric material is

$$V = S_v \cdot p \cdot d$$

where

S_v = voltage sensitivity of the material (Volt*meter/ Newton)

p = pressure (Newton/ meter^2) (the scalar quantity of the tensor format stress T)

d = Thickness of the material (meter).

2.2.4. Optical sensors

Several types of optical sensors are on the market and for research, including photoconductive devices [15], photovoltaics [16], photodiodes [17], phototransistors [18], Michelson interferometer [19] *etc*. Among which, Fabry-Perot sensors [20] are used to detect small displacement with high precision, operating with light interference phenomenon.

The cavity with separation d selects which frequencies may oscillate inside the cavity, (q is the mode number and λ is the wavelength of light),

$$d = \frac{\lambda_1}{2} q$$

$$d = \frac{\lambda_2}{2} (q + 1)$$

with $\lambda = \frac{c}{n\nu}$, where c is speed of light in vacuum, n is refractive index, we have

$$\nu_1 = q \frac{c}{2nd}$$

$$\nu_2 = (q + 1) \frac{c}{2nd}$$

Consequently, we get the free spectrum range (*FSR*) $\Delta\nu = \frac{c}{2nd}$ for the transmitted light spectrum. Whatever may cause change in the cavity separation (mirror movement), may be detected by the change of *FSR*. These include strain, force, pressure, and temperature.

2.2.5. Magnetic sensors

There are many types of magnetic sensors on the market, including anisotropic magnetoresistive (AMR) sensors [21, 22], which are based on spin-orbit scattering; giant magnetoresistive (GMR) sensors [23], which are based on spin accumulation; tunneling magnetoresistive (TMR) sensors [24], which are based on dependent tunneling effect *etc*. Among which, magnetism based tactile sensors measure the change in flux density as a result of the applied force. The flux measurement can be made either by utilizing Hall effect [25, 26] or magnetoresistive (MR) [27] effect. The underlying working principle of which is Lorentz force. The above-mentioned AMR, GMR, and TMR sensors all detect magnetic field, while Hall effect sensors and MR sensors detect the secondary field as magnetic flux density.

2.3. Comparison of Different Sensor Types

Now we have enough information to compare each of the sensor types mentioned in Chapter 2.2. in terms of the specifications for tactile sensing. A summary of the comparison is listed below.

Table 4 Comparison of the reviewed sensing techniques [3, 4]

Sensor Type	*Merits*	*Demerits*
Piezoresistive (strain gauge)	1. High sensitivity	1. Stiff and fragile
	2. Low cost	2. Non-linear response
	3. Low noise	3. Hysteresis
	4. Simple electronics	4. High temperature dependence
	(high spatial resolution)	5. Signal drift (low repeatability)
	5. 3D force sensing possible	6. Relatively costly materials and fabrication techniques
Piezoelectric	1. High sensitivity	1. Temperature sensitive
	2. Well suited for dynamic applications	2. Lacks robust electrical connections
	3. High bandwidth	3. Decay of static response (poor static sensing)
	4. Robust and chemically resistant	4. Not stretchable
Capacitive	1. Sensitive	1. Cross-talk between sensor elements (noise)
	2. Low cost (simple fab)	2. Hysteresis

	3. Suitable for static and dynamic signal	3. Relative complex circuitry
	4. Temperature independent	4. Parasitic capacitances
	5. Small sizes and high spatial resolution possible	5. Sensitive to electromagnetic interference
	6. 3D force sensing possible	
Magnetic	1. High sensitivity	1. Restricted to non-magnetic medium
	2. Good dynamic range	2. Complex computations
	3. Robust	3. Somewhat bulky
	4. No mechanical hysteresis	4. High power consumption
Optical-based	1. Good sensing range	1. Bulky
	2. Reliable/ repeatable	2. Non-conformal

References

[1] Najarian, S., Dargahi, J., & Mehrizi, A. A. (2009). *Artificial tactile sensing in biomedical engineering* (pp. 105-22). New York: McGraw-Hill.

[2] Dahiya, R. S., Valle, M., (2013). *Robotic tactile sensing technologies and systems*. New York: Dordrecht Heidelberg.

[3] Yousef H, Boukallel M and Althoefer K 2011 *Tactile sensing for dexterous in-hand manipulation in robotics: a review. Sensors Actuators* A **167** 171–87

[4] R.S. Dahiya, G. Metta, M. Valle, G. Sandini, Tactile sensing—from humans to humanoids, *IEEE Trans. Robot.*, 26 (1) (2010), pp. 1–20

[5] H. Liu, P. Meusel, and G. Hirzinger, "A tactile sensing system for the DLR three-finger robot hand," in *Proc. Int. Symp. Meas. Control Robot.*,1995, pp. 91–96.1837

[6] M. A. Diftler, R. Platt, Jr., C. J. Culbert, R. O. Ambrose, and W. J. Bluethmann, "Evolution of the nasa/darpa robonaut control system," in *Proc. IEEE Int. Conf. Robot. Autom.*, 2003, pp. 2543–2548

[7] Z. Chu, P. M. Sarro, and S. Middelhoek, "Silicon three-axial tactile sensor," *Sens. Actuators A*, vol. 54, pp. 505–510, 1996

[8] B. L. Gray and R. S. Fearing, "A surface micromachined microtactile sensor array," in *Proc. Int. Conf. Robot. Automat.*, Minneapolis, MN, 1996, vol. 1, pp. 1–6

[9] R. J. D. Souza and K. D. Wise, "A very high density bulk micromachined capacitive tactile imager," in *Proc. Int. Conf. Solid-State Sens. Actuators,Transducers*, Chicago, IL, 1997, pp. 1473–1476

[10] P. A. Schmidt, E. Mael, and R. P. Wurtz, “A sensor for dynamic tactile information with applications in human-robot interaction & object exploration,” *Robot. Autonomous Syst.,* vol. 54, pp. 1005–1014, 2006

[11] E. S. Kolesar, R. R. Reston, D. G. Ford, and R. C. Fitch, “Multiplexed piezoelectric polymer tactile sensor,” *J. Robot. Syst*., vol. 9, no. 1, pp. 37–63, 1992.

[12] J. Dargahi, M. Parameswaran, and S. Payandeh, “A micromachined piezoelectric tactile sensor for an endoscopic grasper—theory, fabrication and experiments,” *J. Microelectromech. Syst*., vol. 9, no. 3, p329-335, 2000

[13] Y. Yamada, T. Maeno, I. Fujimoto, T. Morizono, and Y. Umetani, “Identification of incipient slip phenomena based on the circuit output signal of PVDF film strips embedded in artificial finger ridges,” in *Proc. SIC Robots Syst*., 2005, pp.2638-2643

[14] B. Choi, H. R. Choi, and S. Kang, “Development of tactile sensor for detecting contact force and slip,” in *Proc. IEEE/RSJ Int. Conf. Intell. Robots Syst*., 2005, pp. 2638-2643

[15] Barg, J.E.; Jin, X.; Wiltshire, M.; Abolhasani, M.; Holzman, J.F., "Photoconductive sensors for distributed optical sensing," in *Electrical and Computer Engineering (CCECE), 2010 23rd Canadian Conference on*, vol., no., pp.1-4, 2-5 May 2010

[16] Shahino Mah Abdullah. "Organic Semiconductors: Applications in Solar Photovoltaic and Sensor Devices" *Materials Science Forum* Vol. 737 (2013)

[17] O’Toole, M. and Diamond, D. “Absorbance Based Light Emitting Diode Optical Sensors and Sensing Devices,” *Sensors* 2008, 8, 2453-2479

[18] Refaat, Tamer F., et al. "AlGaAsSb/InGaAsSb phototransistors for 2-μm remote sensing applications," *Optical Engineering* 43.7 (2004): 1647-1650.

[19] Tian, Z., Scott, S.Y., and Loock, H.P., "Refractive index sensor based on an abrupt taper

Michelson interferometer in a single-mode fiber." *Optics letters* 33.10 (2008): 1105-1107.

[20] Murphy, Kent A., et al. "Quadrature phase-shifted, extrinsic Fabry–Perot optical fiber sensors." Optics Letters 16.4 (1991): 273-275.

[21] S. Tumanski, “Thin Film Magnetoresistive Sensors.” Bristol, U.K. IOP Publishing, 2001

[22] E. Zimmermann, A. Verweerd, W. Glaas, A. Tillmann, and A. Kemna,“An AMR sensor-based measurement system for magnetoelectrical resistivity tomography,” *IEEE Sensors J.*, vol. 5, pp. .233–241, 2005.

[23] L. Xu, H. Yu, S.-J. Han, S. Osterfeld, R. L. White, N. Pourmand, and S.X. Wang, “Giant magnetoresistive sensors for DNA microarray,” *IEEE Trans. Magn.*, vol. 44, pp. 3989–3991, 2008

[24] Albon, C. and Weddemann, A. and Auge, A. and Rott, K. and Hütten, A., "Tunneling magnetoresistance sensors for high resolutive particle detection," *Applied Physics Letters,* 95, 023101 (2009)

[25] E. Torres-Jara, I. Vasilescu, and R. Coral, “A soft touch: Compliant tactile sensors for sensitive manipulation,” *CSAIL, Mass. Inst. Technol.,* Cambridge, MA, Tech. Rep., 2006G

[26] L. Jamone, G. Metta, F. Nori, and G. Sandini, “James: A humanoid robot acting over an unstructured world,” in *Proc. 6th IEEE-RAS Int. Conf. Humanoid Robots*, Genoa, Italy, 2006, pp. 143–150

[27] T. J. Nelson, R. B. V. Dover, S. Jin, S. Hackwood, and G. Beni, “Shear sensitive magnetoresistive robotic tactile sensor,” *IEEE Trans. Magn.,* vol. MAG-22, no. 5, pp. 394–396, Mar. 1986.

Chapter 3: CAPACITIVE SENSOR DESIGN

From Table 4, it is clear that optical-based sensors and magnetic sensor cannot be used in robotic sensor, since currently available devices are too bulky for our grasper tip. Piezoresistive sensors have the issue of high temperature dependence, while most piezoelectric sensors lack the ability of sensing static force. Although capacitive sensors are susceptible to noise and parasitic capacitance, and the need of a complex readout circuit, those issues can be solved by using a capacitance to digital converter (CDC) and differential design.

3.1. Literature Review and Design Insights of Capacitive Sensor

3.1.1. Review of 3-axis capacitive sensors

Figure 5-8 show the schematic view of four state-of-the-art capacitive sensors which are capable of sensing both normal and shear forces [1-4].

Cheng *et al* [1] presents a polymer-based three- axial capacitive sensing array which is realized by micromachining and flexible printed circuit board (PCB) technique. This design is capable of sensing both normal and shear force.

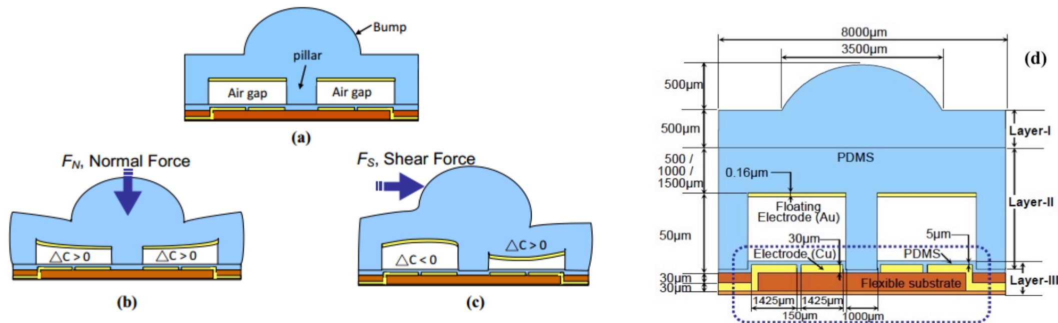

Figure 5 Schematic of a shear stress sensing element (a) without applied forces, (b) with a normal force, (c) with a shear force (d) detailed design of the sensing element by Cheng *et al*[1]

Dobrzyns *et al* [2] developed a flexible-substrate-based three-axial force sensor as depicted in Fig. 6. This sensor design is comprised of finger-shaped capacitive electrodes and the three layer of polymeric packaging (polymide, parylene-C, and polydimethylsiloxane) makes the proposed sensor fully flexible and elastic.

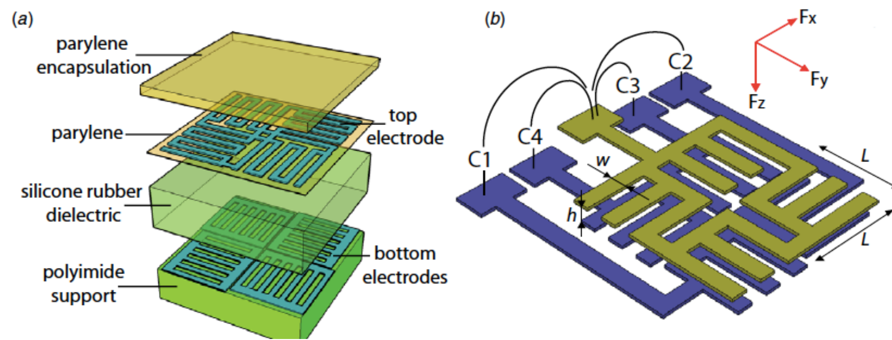

Figure 6 (a) Design of the capacitive sensor, with top and bottom electrodes embedded in three layers of polymeric packaging (b) the schematic of the sensing element: the finger shape electrodes form four unit capacitors C_1–C_4, which can support 3-axis sensing by Dobrzyns *et al* [2].

Surapaneni *et al* [3] designed a flexible tactile imager (FTI) which utilizing microelectromechanical systems (MEMS) and FPCB techniques, comprising a flexible array of normal and shear stress sensors. The normal stress is measured by the net capacitance of the cell and the shear stress is calculated by the overlap difference of the floating electrodes with respect to the bottom electrodes. One thing to notice is that they made use of the floating electrodes for the purpose of simplifying the circuit.

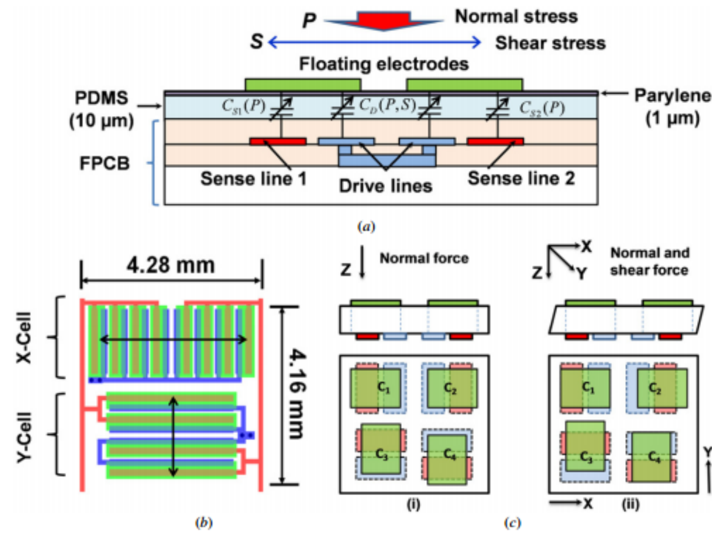

Figure 7 (a) Cross section view of the sensing cell (b) Each unit cell consists of an X-cell and a Y-cell which measure normal stress and shear in x- and y-directions represented by the arrows, respectively (c) sensing schematics: capacitances C_1 and C_2 belong to the X-cells C_3 and C_4 belong to the Y-cell. (i) A sensing cell under only normal force and (ii) with both shear and normal force [3].

Brookhu *et al* [4] have fabricated a silicon force–torque sensor which consists two parts can detect both normal and shear stress. The top part consists of equally distributed silicon pillars and the bottom part consists of electrodes for capacitive read-out. The normal force can be detected by a change in the gap from the compression of the silicon pillars and the shear force can be determined by the sideways bending of the silicon pillar. The comb structures enable the measurement of shear force as well as all the torque components.

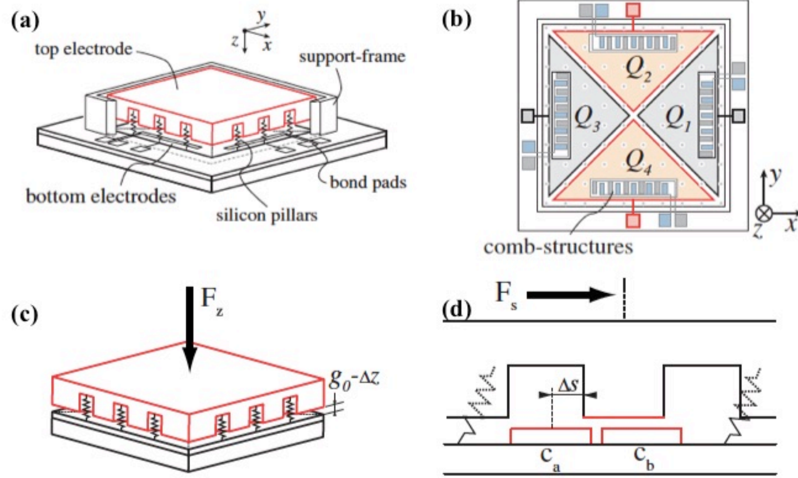

Figure 8 (a) Schematic of the sensing structure (b) configuration of the bottom electrode: the triangular shaped electrodes are used to measure F_z, M_x and M_y, the comb structures are used to measure F_x, F_y, and M_z. (c) normal force sensing: capacitance change because of the decreased gap distance (d) shear force sensing: differential change in capacitance between electrodes C_a and C_b with respect to the top electrode because of the silicon pillars bending by Brookhu *et al* [4]

3.1.2. Design insights

The first design insight from literature review is to design a differential capacitive sensor, which is widely employed for the measurement of linear and angular displacement, pressure, and acceleration. The differential design benefits from its compensation of common mode noise or errors, which can include tilting, temperature variation, some sources of electrical noise, humidity, and pressure.

A typical differential capacitive sensor is made of two capacitors, C_1 and C_2, the change of the input physical signal will cause one capacitance (C_1) to increase and the other capacitance to decrease (C_2), also known as push-pull capacitive sensors. From section 3.2.2, for a simple parallel capacitor,

$$C_0 = \frac{\varepsilon_0 \varepsilon_r A}{d}$$

If the parameter that changes with the physical quantity being sensed is either the area *A* or the relative permittivity ε_r, then

$$C_1 = C_0(1 + kx)$$

and

$$C_2 = C_0(1 - kx)$$

The difference is what we care about

$$\Delta C = C_1 - C_2 = 2C_0 kx$$

as well as the ratio

$$\frac{C_1}{C_2} = \frac{1 + kx}{1 - kx} = 1 + \frac{2kx}{1 - kx} \approx 1 + 2kx$$

where ΔC is the nominal value of sensor capacitance C_1 and C_2, k is the transformation constant of the sensor and x is the physical quantity being sensed.

From the equations, it is clear that the variances of temperature, pressure effect to dielectric material can be compensated by ratiometric measurement.

The second design insight from literature review is to combine the flexible microelectromechanical systems (MEMS) with flexible printed circuit board (FPCB) techniques.

And the third design insight is to use unconnected floating electrodes as proposed in [3] with the beneficial of eliminating the need for pattering electrical wiring and thus simplifying the design and ultimately making the integration easier.

Three versions of capacitive sensors have been proposed. First, we investigated the comb drive

model but found that its circuit and wiring are very complicated. Then we proceeded to investigate the joystick structure for its enhanced simplicity and smaller footprint, and finally investigated a single-sided joystick model for ease of integration with the surgical system.

3.2. Comb Drive Model

3.2.1. Schematic of comb drive design

Figure 9 shows the schematic of the comb drive design.

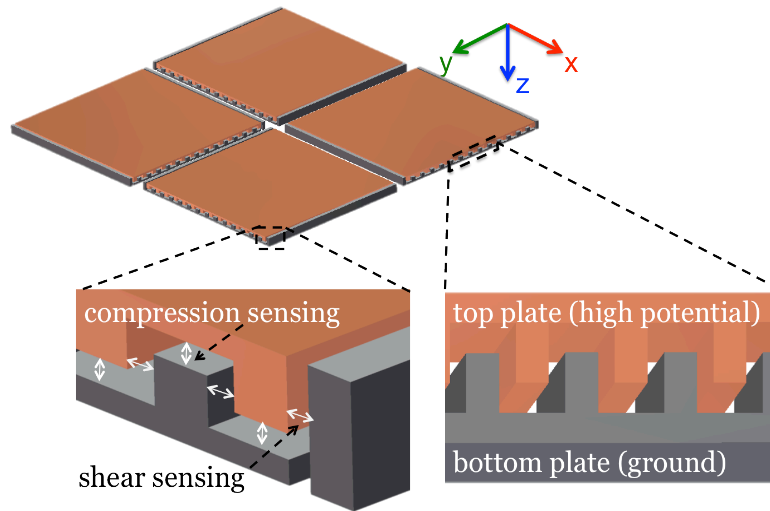

Figure 9 Schematic drawing of comb drive model for both compression sensing and shear sensing

3.2.2. Sensitivity calculation

Fig. 10 shows a typical circuit layout for connecting the differential sensor to a read out circuit. The output voltage is read as

$$V_o = \frac{2\Delta C}{2C_0 + C_p} V_m$$

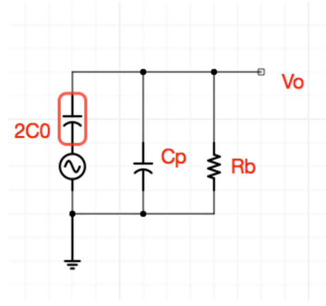

Figure 10 Read-out circuit for a differential capacitive sensor

For simplicity, we will consider only one single finger instead of N number of fingers in the structure, then the sensitivity is given as:

$$\frac{\partial V}{\partial F}=\frac{\partial V}{\partial C}\frac{\partial C}{\partial x}\frac{\partial x}{\partial F}=\frac{2}{2C_0+C_p}V_m\bullet\frac{\varepsilon_0\varepsilon_r A_{overlap}}{(g-x)^2}\bullet\frac{l}{GA_{grasper}}$$

where C_0 is the nominal capacitance, C_p is the parasitic capacitance of the read-out circuit, V_m is the activation voltage for the sensor, ε_0 is the permittivity of air, and ε_r is the relative permittivity of the dielectric material, $A_{overlap}$ is the overlap area of the two electrodes which form the capacitor, g is the gap distance between the two electrodes, and G is the shear modulus of the material.

Rearranging and simplifying the formula as follows:

$$\frac{\partial V}{\partial F}=\frac{2}{2C_0+C_p}\frac{(1+2v)\varepsilon_0\varepsilon_r}{E}\frac{A_{overlap}}{(g-x)^2}\frac{1}{A_{grasper}}V_m$$

We can interpret the equation in terms of circuit capability, material property, sensor geometry, and the grasper size:

1) The first term only carries the nominal capacitance C_0 and the parasitic capacitance C_p, which is a circuit related only parameter. By minimizing the parasitic capacitance, we can have better sensitivity.

2) The second term $\frac{(1+2v)\varepsilon_0\varepsilon_r}{E}$ has parameters only related to the dielectric material, the Young's modulus, the Poisson ratio, and the relative permittivity. By carefully choosing the material, we can have optimal sensitivity.

3) The third term $\frac{A_{overlap}}{(g-x)^2}$ has parameters only related to the geometry of the designed sensor, giving us hint how to optimize the width, length, and gap distance of the comb drive.

Assuming the parasitic capacitance very small, we have the sensitivity as:

$$\frac{\partial V}{\partial F} = \frac{2(1+v)}{E} \frac{g}{(g-x)^2} \frac{1}{A_{grasper}} V_m$$

We can have the conclusion as:

a) If there is no applied force, displacement x equals zero, we would have $dV/dF = 0.2V_m$

b) We can further improve the sensitivity by making the gap g small, and overlap area $A_{overlap}$ large.

3.2.3. Results and discussion

Ignoring the read-out circuit for now, we have the sensitivity as:

$$\frac{\partial C}{\partial F} = \frac{\partial C}{\partial x}\frac{\partial x}{\partial F} = \frac{\varepsilon_0 \varepsilon_r l_p t}{(g-x)^2} \bullet \frac{l}{GA_{grasper}}$$

plug into the values of these parameters, the calculated sensitivity is

$$\frac{\partial C}{\partial F} = 8.28 fF/N$$

while using the COMSOL simulation, as shown below in Fig. 11, the sensitivity is 3 *fF/N*.

$$resolution = \frac{noise}{sensitivity} = \frac{20aF}{8.28 fF/N} = 2.4mN$$

The resolution used here is the minimum resolvable force while the noise value comes from a capacitance to digital converter (CDC) AD7746 readout circuit chip (Chapter 4) which we use to integrate the sensor to the grasper of the operating medical tool.

So far, we have met the resolution requirements for both shear and normal force. However, the footprint is relatively larger as well as the wiring is very complicated, we need to change the model.

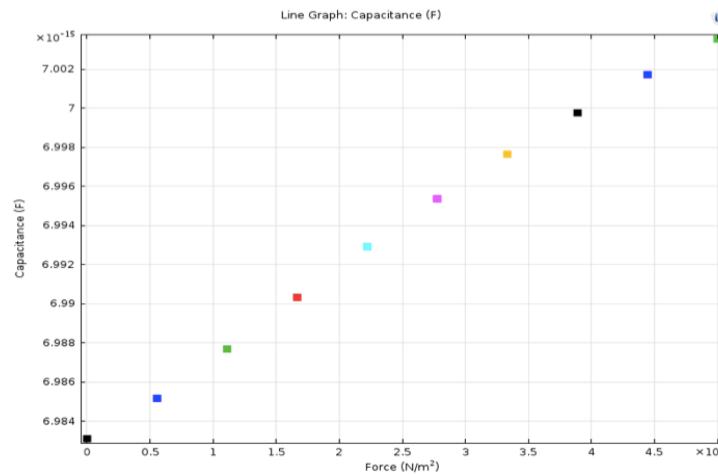

Figure 11 COMSOL simulation capacitance vs force, leading to the sensitivity be 3 fF/N

3.3. Joystick Model

3.3.1. Schematic of joystick design

The joystick capacitive sensor is designed as this: we have the PDMS as the elastic material embedded between two layer of Au conducting plates, forming the capacitance. The area insides red line is the bottom plate, while the area insides the grey dotted line is the top plate (Fig. 12). The top plate possesses five parts, the center square plate, and the surrounded four trapezoids

working as differential shear force detectors. The working principle is as follows: any force can be divided into three directions, *x, y, z* with z direction force be normal force, and *x, y* direction force be shear force. After applying a force, we will have displacement in x and y direction and decrease distance between the top and bottom plates because of the normal force. All of these make the capacitances change as indicated by Fig. 12 (*b*).

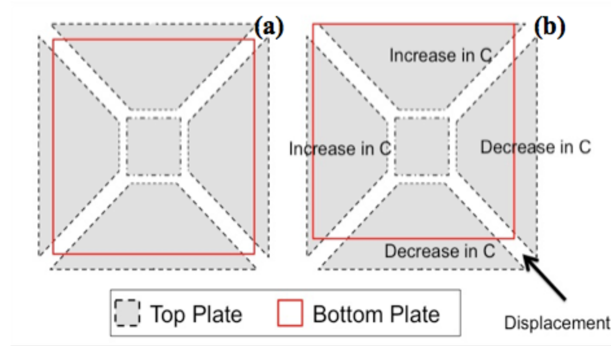

Figure 12 Working principle of joystick model. The center plate can detect normal force while the surrounded four parts of electrodes are capable of sensing shear force.

The schematic drawing for the trapezoid is plotted in Fig. 13, where x_0 is the original overlap distance with the underlying square, S_0 and S_2 are the designed length of the trapezoid and h is the height of the trapezoid.

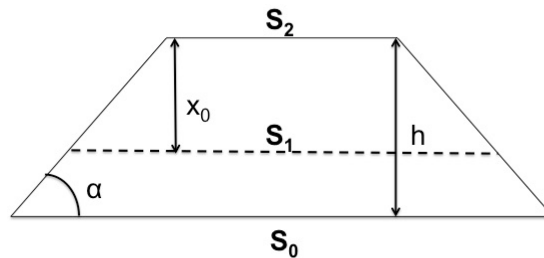

Figure 13 Schematic drawing for one trapezoid in the capacitive sensor design

3.3.2. Sensitivity calculation

S_0, S_1, and S_2 have the relationship:

$$S_0 = S_2 + 2h\cot\alpha \Rightarrow S_2 = S_0 - 2h\cot\alpha$$
$$S_1 = S_2 + 2x_0\cot\alpha \Rightarrow S_1 = S_0 - 2(h - x_0)\cot\alpha$$

the overlap area is

$$A_{overlap} = \frac{1}{2}(S_1 + S_2)x_{\mathbf{0}} = (S_0 - 2h\cot\alpha)x_0 + (\cot\alpha)x_0^2$$

then we can calculated sensitivity *dc/dx* as

$$\frac{dc}{dx} = \frac{2\varepsilon}{d}\left[S_0 - 2\cot\alpha(h - x_0)\right]$$

Plotting the sensitivity with respect to the designing angle α

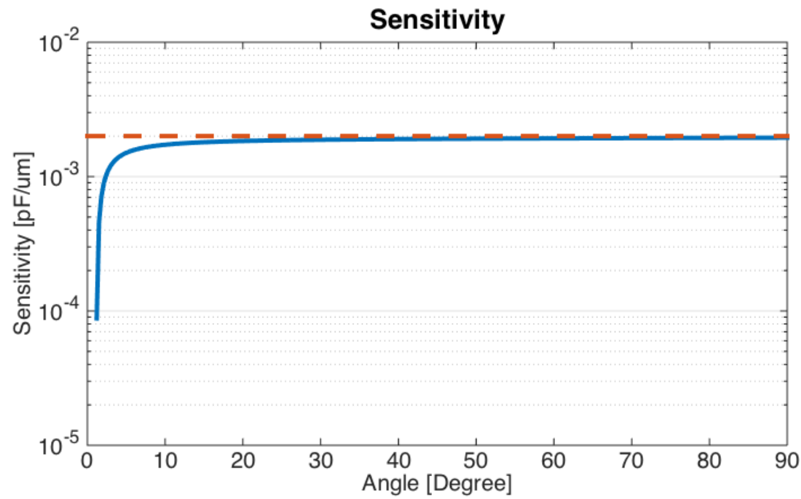

Figure 14 Sensitivity dc/dx with respect to different angle (in degree)

The values show that when the angle is 90 degrees, *dc/dx*= 4.87 *aF/um*, and when the angle is 45 degrees, *dc/dx*= 4.77 *aF /um*. It is easy to see from both the plot and the values that the sensitivity does not change much from angle 45 degrees to 90 degrees, varies only *0.1 aF/um* (*1aF= 1E-15 Farad*). It is reasonable to design the trapezoid with angle 45 degrees for simplicity. Now the simplified sensitivity *dc/dx* is

$$\frac{dc}{dx} = \frac{2\varepsilon}{d}\left[S_0 - 2(h - x_0)\right]$$

The design insight is thus to make overlap x_0 close to the height h.

$$A_1 = a^2$$
$$A_{2,3,4,5} = \left(S_0 - 2h\right)x_0 + x_0^2$$

Looking at the geometry in Fig. 15, naming the center electrode as C_1, the *y*-direction electrodes as C_2 and C_4, the *x*-direction electrodes as C_3 and C_5.

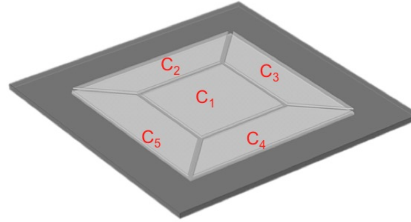

Figure 15 Geometry of the top layer of the joystick model

a. Considering normal force only

For the simulation of the sensor's behavior upon applied load, we assumed a simplified linear elastic stress-strain model. When normal compressive stress F_N is applied to the sensor, the polymer dielectric compresses and the initial distance between the electrodes decreases by Δd, and the Young's modulus E of the polymeric material between the electrodes can be written as

$$E = \frac{F_N / A}{\Delta d / d}$$

where A is the area on which the normal force is applied.

Then we can have the compressed distance d as

$$d' = d - \Delta d = d(1 - \frac{F_N}{AE})$$

$$C = \varepsilon_0 \varepsilon_r \frac{A}{d'} = \varepsilon_0 \varepsilon_r \frac{A}{d}(1 + \frac{F_N}{AE}) \text{ if } \frac{F_N}{AE} \ll 1$$

b. Considering shear force only

We simplify the shear force in positive x direction, and only cause the area of capacitor 3 and capacitor 5 changes:

$$A_5' = (S_0 - 2h)(x_0 + x') + (x_0 + x')^2$$
$$A_3' = (S_0 - 2h)(x_0 - x') + (x_0 - x')^2$$

$$C = \varepsilon_0 \varepsilon_r \frac{A_{3,5}'}{d}$$

By the same token, if we have positive y-direction force, simply change the A_3 and A_5 to be A_2 and A_4.

c. Considering we have both normal and shear force

It is easy to understand that the center square capacitor C_1 and the top and bottom capacitor C_2 and C_4 only influenced by F_N, the value of these capacitors are as follows:

$$C_1 = \varepsilon_0 \varepsilon_r \frac{A_1}{d'} = \varepsilon_0 \varepsilon_r \frac{a^2}{d}(1 + \frac{F_N}{A_1 E}) = \varepsilon_0 \varepsilon_r \frac{a^2}{d} + \frac{\varepsilon_0 \varepsilon_r}{dE} F_N$$
$$C_2 = C_4 = \varepsilon_0 \varepsilon_r \frac{A_2}{d}(1 + \frac{F_N}{A_{trap} E}) = \varepsilon_0 \varepsilon_r \frac{A_2}{d} + \frac{\varepsilon_0 \varepsilon_r}{dE} \frac{A_2}{A_{trap}} F_N$$

the sensitivities are

$$\frac{dC_2}{dF_N} = 2.3 pF / N$$
$$\frac{dC_1}{dF_N} = 2.43 pF / N$$

while C_3 and C_5 are influenced by both F_N and F_s, the capacitance are:

$$C_3 = \frac{\varepsilon}{d}\left[x_0^2 + (S_0 - 2h)x_0\right] + \frac{\varepsilon}{dE} F_N - \frac{\varepsilon(S_0 - 2h)}{A_{grasper} G} F_s + \frac{\varepsilon(S_0 - 2h)}{A_{grasper}^2 EG} F_s F_N$$
$$C_5 = \frac{\varepsilon}{d}\left[x_0^2 + (S_0 - 2h)x_0\right] + \frac{\varepsilon}{dE} F_N + \frac{\varepsilon(S_0 - 2h)}{A_{grasper} G} F_s - \frac{\varepsilon(S_0 - 2h)}{A_{grasper}^2 EG} F_s F_N$$

Initial Cap Constant	Normal Force Only	Shear Force Only	Coupling Component

Here we use ε to replace $\varepsilon_0 \varepsilon_r$, the differential capacitance is thus

$$C_5 - C_3 = 2\frac{\varepsilon(S_0 - 2h)}{A_{grasper}G}F_s - 2\frac{\varepsilon(S_0 - 2h)}{A_{grasper}^2 EG}F_s F_N$$

Gives us both the direction (either the C_5-C_3 is positive or negative) and the amplitude. As a result, the shear force sensitivity is

$$\frac{dC}{dF_S} = 2\frac{\varepsilon(S_0 - 2h)}{A_{grasper}G} = 3.6\, fF / N$$

For the above calculation, F_s is by nature F_x. Any force can be divided into three directions, *x, y,* and *z*. For example, the above calculation for *x*- direction capacitances C_3 and C_5 were only considered influenced by normal force and *x*- direction force, not *y*- direction force. However, by considering both *x* and *y*- direction force, there is an additional displacement in y, causing no change in C_3 and C_5. In conclusion, the calculation above can be applied to any case.

3.3.3. Optimal design parameters

Figure 16(*a*) shows the change of capacitance with normal force with different materials: polydimethylsiloxane (PDMS), silicon dioxide, silicon nitride, polyimide, praylene C, and polyethylene. From the plot, we can notice the sensitivity (*dC/dF*) varies 5 orders of magnitude, with PDMS 2 orders more sensitive than the second silicon dioxide. The large difference comes from Young's modulus of each material. Detailed explanation will be given in section 3.3. We pick PDMS to be the dielectric material as a result.

Fig. 16(*b*) shows the capacitance change linearly with electrode dimensions a, which is the size of the center electrode shown in Fig. 16. With larger electrode dimension, we can have more sensitive sensor, unfortunately, the grasper size limits. For a typical grasper tip used in robotic

surgery, its size is 2 millimeter by 10 millimeter. Making the electrode dimension a 500 micrometer to be the optimal parameter we use.

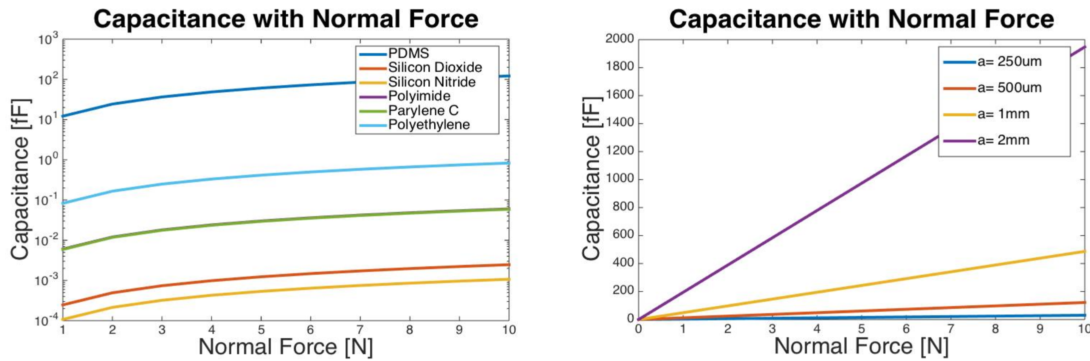

Figure 16 Change of capacitance with compression force 0-10N for (a) different materials, (b) different electrode dimensions with PDMS as the dielectric.

Similarly, Fig. 17 (*b*) shows the change of capacitance with shear force (shear sensitivity) for different materials, (*b*) shows the shear capacitance with different electrode dimensions. The conclusion is the same as for normal force: use PDMS as the dielectric material and the designed parameter value is *a*= 500 *um*.

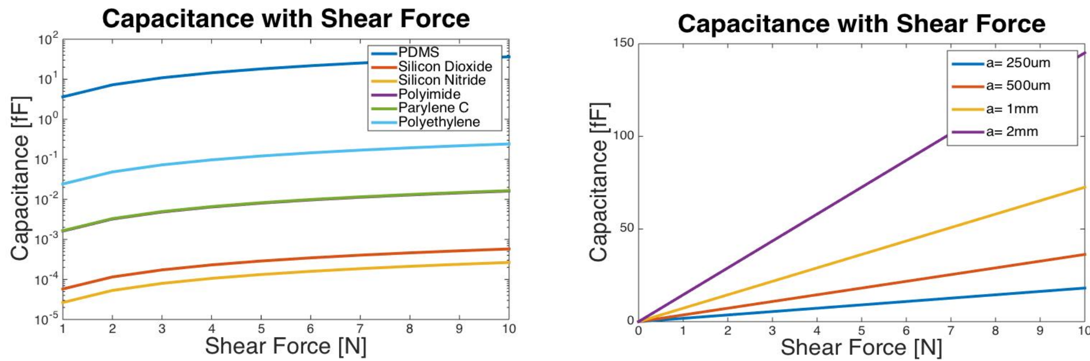

Figure 17 Change of capacitance with shear force 0-10N for (a) different materials, (b) different electrode dimensions with PDMS as the dielectric.

3.3.4. Fabrication process

The fabrication process is detailed in Fig. 18.

Step 1: starting with a silicon substrate, and PECVD 5 micrometer oxide (SiO_2)(*a*). The front side oxide will act as etch stop for the FDRIE step while the backside oxide will act as insulating layer for the plating step.

Step 2: using CHA to deposit a Ti/Cu/Ti seed layer, and then we can electroplate a 5 micrometer Au layer (*b*). This step is designed to create a bondable surface for assembly and back-end processing. The bottom 20-nanometer Ti layer works as the adhesion layer, while the top 1.5-micrometer Ti layer serves as a mechanical robust, biocompatible electrode. The Au layer is used to be bonded as a biocompatible electrode.

Step 3: spin coating a 25-um PDMS layer (c). The recipe is under examination so far, but ideally, we spin on a 5-mL 5:1 ratio PDMS, with spinning condition as: 500 rpm at 100 rpm/s for 5 seconds, and then 2000 rpm at 300 rpm/s for 30 seconds, and finally 25 rpm at 100 rpm/s for 15 seconds to stop. We can use the Q-tip with acetone to remove the edge bead.

Step 4: lithographically defining top plate (*d*). As a standard routine, we put the wafer in HMDS for 10 minutes before spin on KMPR 1005. The recipe is 500 rpm at 100 rpm/s for 5 seconds, 2000 rpm at 300 rpm/s for 30 seconds and 25 rpm at 100 rpm/s for 15 seconds. Next, soft bake on the hotplates for 5 minutes at 100 degree. After exposure and post bake at 100 degree for 2 minutes, we use SU-8 to develop for 2 minutes and 30 seconds with strong agitation.

Step 5: electroplate another 5-um Au layer (*e*).

Step 6: striping the plating mold and the seed layer (*f*).

Step 7: removing the substrate by grinding to the silicon dioxide layer, and then use Hydrogen Fluoride (HF) to etch away remaining SiO_2.

Step 8: after dicing the wafer, we can flipchip and solderbump to the flexible printed circuit board (FPCB).

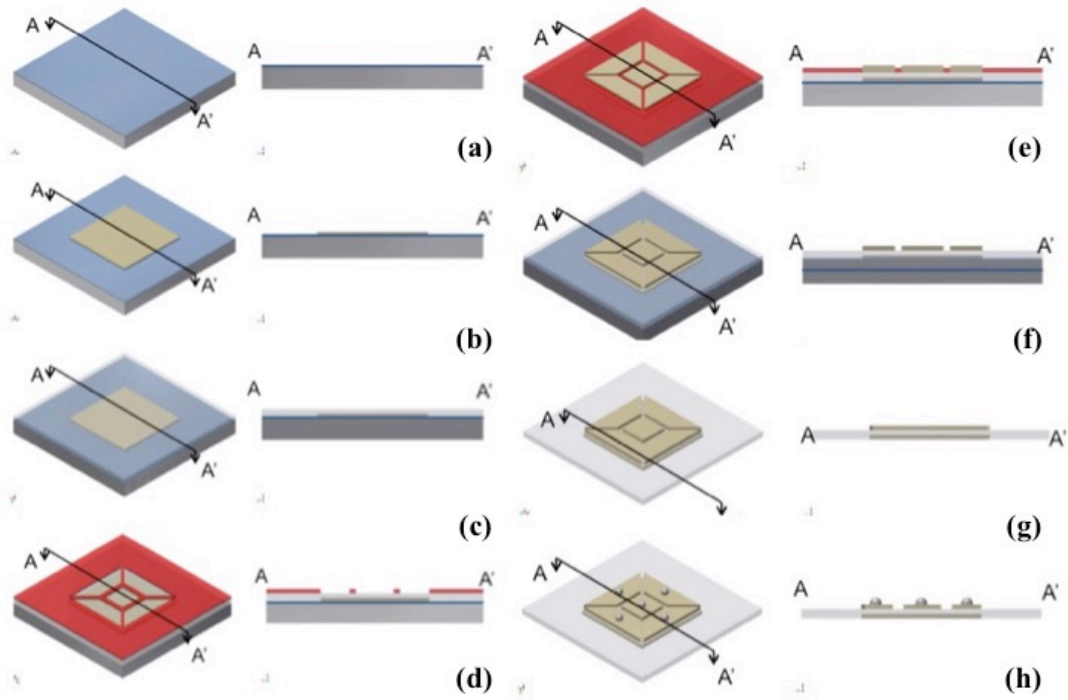

Figure 18 Fabrication process (a) PECVD SiO2 (b) Au deposition of bottom layer (c) PDMS coating (d) photolithography to define top layer (e) Au deposition of top Au layer (f) strip plating mold (g) substrate removal (h) backend process to integrate to FPCB

The prime problem with the fabrication process is the height control of PDMS. For a robust and repeatable manufacture, the thickness must be both accurately controllable and uniform across the entire film. The spin-coating technique is employed to meet the requirement of a uniform thickness PDMS layer.

Assume that we pour the PDMS on the wafer as a cylinder with height h_0 and diameter d. By using Navier-Stokes equation, the height of the PDMS can be derived as:

$$\frac{1}{h_t^2}-\frac{1}{h_0^2}=\frac{4\rho\omega^2 t}{3\mu}$$

where h_t is the height of the PDMS, h_0 is the initial height of the poured PDMS, ρ is the density of the PDMS, ω is the spin speed, t is the spin time, and μ is the dynamic viscosity of PDMS.

From the expression, we notice that, the final height is uniform, not related to the radial location or the size of the film (the size of the wafer). However, it is sensitive to the initial height. If we make $h_t \gg h_0$, i.e., making the initial pour volume large, the initial height will no longer be an issue.

$$h_t \approx \sqrt{\frac{3\mu}{4\rho\omega^2 t}}$$

However, various factors will affect PDMS's property, including the dynamic viscosity, modulus of elasticity, Poisson's ratio, tensile strength and adhesion energy. For example, the dynamic viscosity increases over time once monomer and cross-linker are mixed. The Young's modulus is sensitive to the temperature and time during curing as well as can increase with the increased ratio of cross-linker to monomer. The remaining issue yet to be adequately resolved are how accurate the height model is and how accurate the properties of the PDMS can be made as desired.

Table 5 shows material properties for silicon dioxide, silicon nitride, polyimide, parylene C, polyethylene, and PDMS. The major difference is their Young's modulus. Besides PDMS, the other five materials all have Young's modulus in GPa range, while what PDMS has Young's Modulus in the MPa range. The sensitivity, shown previously, is inversely proportional to Young's modulus. With all the other parameters equal or close, PDMS exhibits at least two orders of magnitude better sensitivity. From resolution point of view, we expect only PDMS and Polyethylene (PE) can meet the requirement of less than 1N resolution (the noise used to calculate resolution is 20 aF from AD7746 datasheet [5]).

Table 5 Material properties

Material	ε_r	Young's modulus (GPa)	Poisson ratio	Normal sensitivity (fF/N)	Shear sensitivity (fF/N)	Normal resolution (N)	Shear resolution (N)
Silicon Dioxide	3.9	70	0.17	2.50e-04	5.70e-05	8.00	351
Silicon Nitride	7.5	310	0.24	1.10e-04	2.66e-05	1.82	752
Polyimide	3.4	2.5	0.34	6.02e-03	1.61e-03	3.32	124
Parylene C	3.2	2.4	0.4	5.90e-03	1.65e-03	3.39	121
Polyethylene	2.25	0.12	0.46	8.30e-02	2.42e-02	0.241	0.826
PDMS	2.75	1.00e-03	0.49	12.2	3.63	1.64e-03	5.51e-03

3.4. Single-sided Sensor Model

3.4.1. Schematic of single-sided sensor design

The single-sided capacitive sensor is designed for easier integration with the surgical system. The sensor design is described in Fig. 19: we have the PDMS as the elastic material embedded between two layers of Au conducting plates, forming the capacitance. The area insides red line is the bottom plate, while the area insides the grey dotted line is the top plate. The top plate possesses seven parts, the center plate for excitation single input, and the surrounding four rectangular plates working as differential shear force detectors. The two square plates are used for normal stress testing. The working principle is as follows: any force can be divided into three directions, x, y, and z with z direction force being normal force, and x, y direction force being shear force. After applying a force, we will have displacement in x and y direction and decrease distance between the top and bottom plates because of the normal force. The details will be further discussed in the next section when calculating sensitivity.

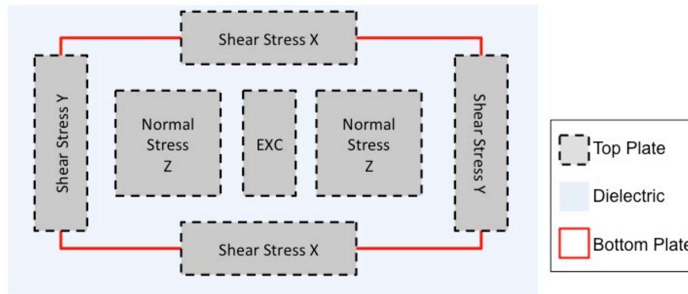

Figure 19 Schematic for single-sided capacitive sensor

3.4.2. Sensitivity calculation

a. Considering normal force only

Figure 20 shows how capacitance will change with normal force. It is clear that the two capacitors corresponding to the normal force are linked in series. $C_z = \frac{C_1 C_2}{C_1 + C_2}$, with the square plate area being S^2 and the compressed distance being d', $C_1 = C_2 = \frac{\varepsilon S^2}{d'}$, leading to $C_z = \frac{\varepsilon S^2}{2d'}$ [Equation set 1].

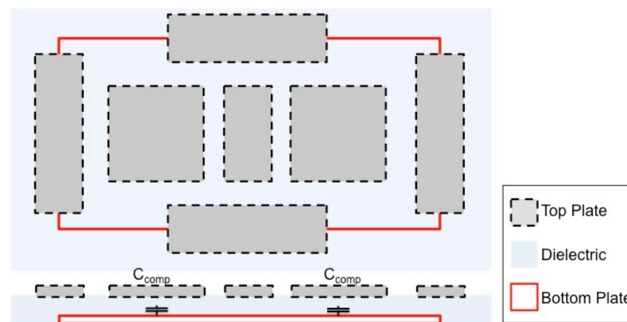

Figure 20 Illustration of how capacitance change with normal force

By definition,

$$\sigma = \frac{F}{A} = E\varepsilon = E(\frac{d-d'}{d}) = E(1-\frac{d'}{d})$$

$$d' = d(1-\frac{F}{AE})$$

[Equation set 2]

where A is the area of the sensor over which force is applied. For the case where sensor width is 3 millimeters, and sensor length is 6 millimeters, we have $A = 18mm^2$.

Combining equation set [1] and [2], we can have

$$C_z = \frac{\epsilon S^2}{2d(1 - \frac{F}{AE})}$$

$$F_{normal} = AE(1 - \frac{\epsilon S^2}{2dC})$$

when $F \ll AE = 180\ N$ (with $A=18mm^2$, $E=10MPa$)

$$C_z \cong \frac{\epsilon S^2}{2d}(1 + \frac{F}{AE})$$

$$F_{N_est} = AE(\frac{2dC}{\epsilon S^2} - 1)$$

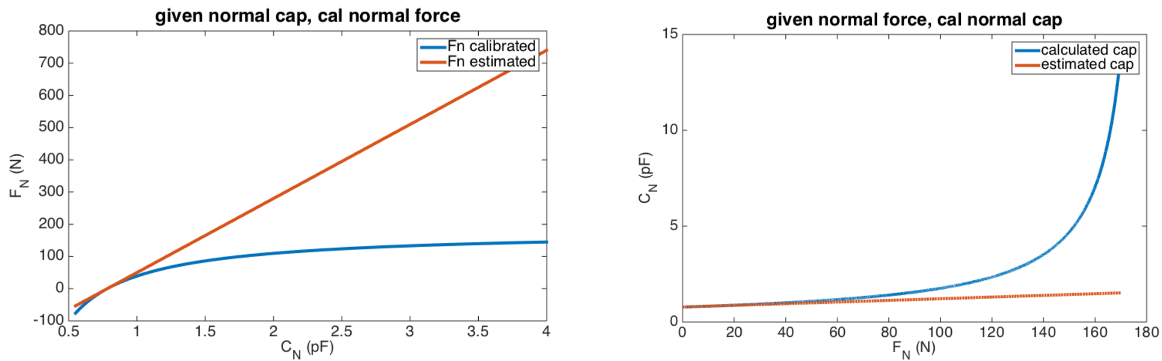

Figure 21 Comparison between estimated value and the accurate value from complete analytical mode for calculation of normal force given normal capacitance, and calculation of normal capacitance given normal force.

Figure 21 shows the comparison between the linear estimated force value and the non-linear calculated force value given the capacitance as well as the comparison between the estimated capacitance value and the calculated capacitance value given the force value. It is clear that the estimation is sufficient valid till 40 Newton, not valid for larger force. However, one thing worth

mentioning is that, in surgical, the surgeons may only apply up to 20 Newton to carry out the operation. Thus, the estimation is valid for our project.

To consider the baseline capacitance C_0 (under no compression):

$$C_z = \frac{\epsilon S^2}{2d(1 - \frac{F}{AE})} = \frac{C_0}{1 - \frac{F}{AE}}$$

Normal sensitivity is changing with the compression force:

$$\frac{dC}{dF} = \frac{C_0/AE}{(1 - F/AE)^2}$$

As a result, the resolution (=noise/ sensitivity) is changing for normal force due to the nonlinearity of the system.

b. Considering shear force only

Figure 22 shows how capacitance will change with shear force. Consider applying the force in horizontal direction to the right. We will get increase in capacitance from the left capacitor because of increased overlap area, and decrease in capacitance from the right capacitor because of decreased overlap area, while the center capacitance remains the same for unchanged overlap area. From Fig. 22, we can also notice that the capacitors corresponding to the shear force are connected to *CIN(+)* pin, *EXC* pin, and *CIN(-)* pin as differential capacitance. For simplicity purpose, we will use *CIN(±)* and *EXC* to reference these capacitors.

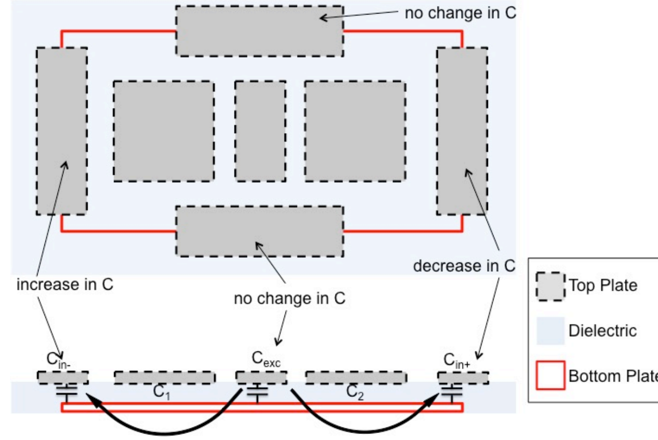

Figure 22 illustration of how capacitance change with shear force

Since there is no compression, *d'*= *d*, the original distance between top and bottom plates, i.e., the PDMS thickness. The size information is marked in Fig. 23.

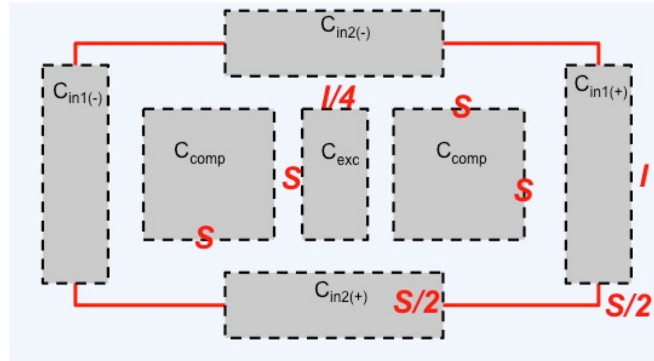

Figure 23 Size information for each fabricated plate

Use y for deflection due to the shear stress, we have the corresponding overlap area for $CIN(\pm)$ and EXC plates as:

$$A_{cin1(\pm)} = (\frac{s}{4} \pm y')l$$

$$A_{exc} = \frac{sl}{4}$$

It is two capacitors in series for the left capacitance C_1 and two capacitors in series for the right capacitance C_2. And the differential capacitance C_y will be the difference between C_1 and C_2.

$$C_1 = \frac{(\frac{\varepsilon A_{exc}}{d})(\frac{\varepsilon A_{in1(-)}}{d})}{(\frac{\varepsilon A_{exc}}{d}) + (\frac{\varepsilon A_{in1(-)}}{d})} = (\frac{\varepsilon}{d})(\frac{A_{exc} A_{in1(-)}}{A_{diff} + A_{in1(-)}})$$

$$C_2 = \frac{(\frac{\varepsilon A_{exc}}{d})(\frac{\varepsilon A_{in1(+)}}{d})}{(\frac{\varepsilon A_{exc}}{d}) + (\frac{\varepsilon A_{in1(+)}}{d})} = (\frac{\varepsilon}{d})(\frac{A_{exc} A_{in1(+)}}{A_{exc} + A_{in1(+)}})$$

$$C_y = C_2 - C_1 = \frac{\varepsilon A_{exc}^2}{d}(\frac{A_{in1(+)} - A_{in1(-)}}{(A_{exc} + A_{in1(+)})(A_{exc} + A_{in1(-)})})$$

$$C_y = -\frac{\varepsilon}{d}(\frac{sl}{4})^2(\frac{2yl}{(\frac{sl}{2})^2 - (yl)^2}) = -\frac{\varepsilon}{2d}(\frac{s^2 ly}{s^2 - 4y^2})$$

By definition, where *A* is the same as mentioned in previous section, the sensor area,

$$\tau = \frac{F}{A} = \gamma G = \frac{y}{d} G$$

$$G = \frac{E}{2(1+\upsilon)}$$

$$C_y = -\frac{\varepsilon l(1+\upsilon)}{AE} F$$

$$y = \frac{F}{AG} d = \frac{2F(1+\nu)}{AE} d$$

$$C_y = -\frac{\epsilon S^2 l}{S^2 - \frac{16F^2(1+\nu)^2 d^2}{A^2 E^2}} \frac{F(1+\nu)}{AE}$$

Rearranging the equation, we can have the quadratic equation

$$\frac{16(1+v)^2 d^2}{A^2 E^2} CapF^2 - \frac{\epsilon(1+v)S^2 l}{AE} F - S^2 Cap = 0$$

To simplify the terms, we have

$$aF^2 + bF + c = 0$$

where

$$a = \frac{16(1+\upsilon)^2 d^2}{A^2 E^2} Cap$$

$$b = -\frac{\epsilon(1+\upsilon)S^2 l}{AE}$$

$$c = -S^2 Cap$$

The unknown variable shear force value is then calculated as:

$$F_{shear} = \frac{-b + \sqrt{b^2 - 4ac}}{2a}$$

There are two estimation can be carried out here, the first is defined as a linear estimation, and the second is defined as a square-root estimation. Details are provided as follows.

i. Linear estimation:

$$C_y = -\frac{\epsilon S^2 l}{S^2 - \frac{16F^2(1+\nu)^2 d^2}{A^2 E^2}} \frac{F(1+\nu)}{AE}$$

Define the variable M as follows, and make the assumption that it is equal to 1.

$$M = \frac{S^2}{S^2 - \frac{16F^2(1+\nu)^2 d^2}{A^2 E^2}} \approx 1$$

Making

$$C_y \approx -\frac{\epsilon(1+\nu)l}{AE} F$$

As a result, the linear approximated force is equal to

$$F_{s_linear} = -\frac{AE}{\epsilon(1+\upsilon)l} C_y$$

This assumption turns out to be a good estimation for force up to 100N, as depicted in Fig. 24. The validation is given to show the calculation for shear capacitance given the information of

shear force. Vice versa, the shear force calculation given the shear capacitance is also displayed in Fig. 25.

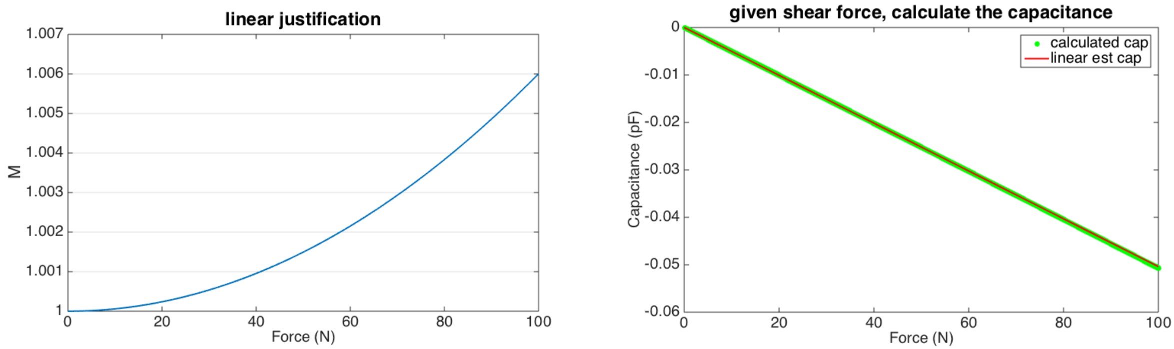

Figure 24 Assumption that $M \approx 1$ ($M = \frac{S^2}{S^2 - \frac{16F^2(1+\nu)^2 d^2}{A^2 E^2}}$) is valid up to 100N from the left figure. Capacitance calculated with and without the assumption is compared shown on the right figure.

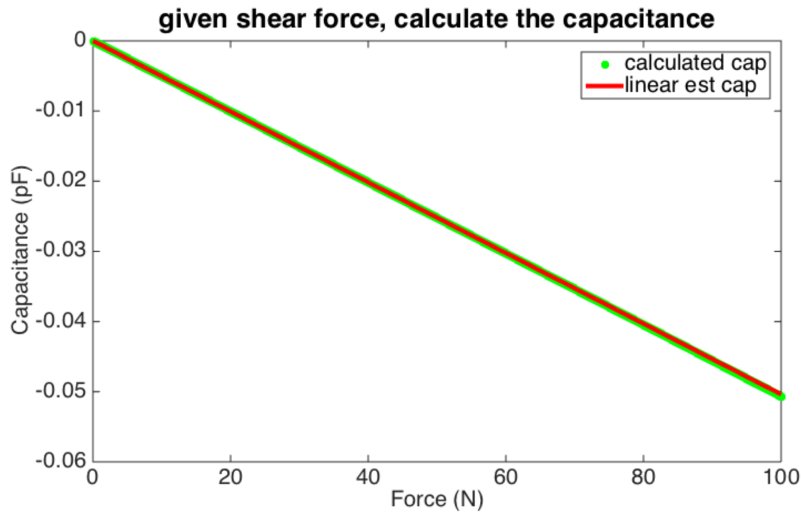

Figure 25 Calculation of shear force given shear capacitance

For shear sensitivity, *dc/df* (using matlab) is a constant number as follows:

The estimated sensitivity =-0.50389 femto-Farad/Newton

The calculated sensitivity =-0.50691 femto-Farad/Newton

ii. Square-root estimation:

$$aF^2 + bF + c = 0,\ F_{shear} = \frac{-b-\sqrt{b^2-4ac}}{2a}$$

when *a* is very small, the assumption is *a=0*, then *bF+c=0* we have

$$\lim_{a\to 0}\left(\frac{-b-\sqrt{b^2-4ac}}{2a}\right) \to \frac{0}{0}$$

Applying L'Hopital differentiate with respect to *a*

$$\lim_{a\to 0}\left(\frac{-b-\sqrt{b^2-4ac}}{2a}\right) = \lim_{a\to 0}\left(\frac{\frac{1}{2}(b^2-4ac)^{-\frac{1}{2}}(-4c)}{2}\right)$$

$$\lim_{a\to 0}\left(\frac{-b-\sqrt{b^2-4ac}}{2a}\right) = \lim_{a\to 0}\left(\frac{-c}{\sqrt{b^2-4ac}}\right) = -\frac{c}{b}$$

$$\lim_{a\to 0}\left(\frac{-b-\sqrt{b^2-4ac}}{2a}\right) = -\frac{AE}{\epsilon(1+\upsilon)l}C_{ap}$$

We are surprised to see this result matches with the linear approximation!

To summarize and plot the square-root estimation, linear estimation, and the calculated shear force given shear capacitance in one graph, we have Fig. 28.

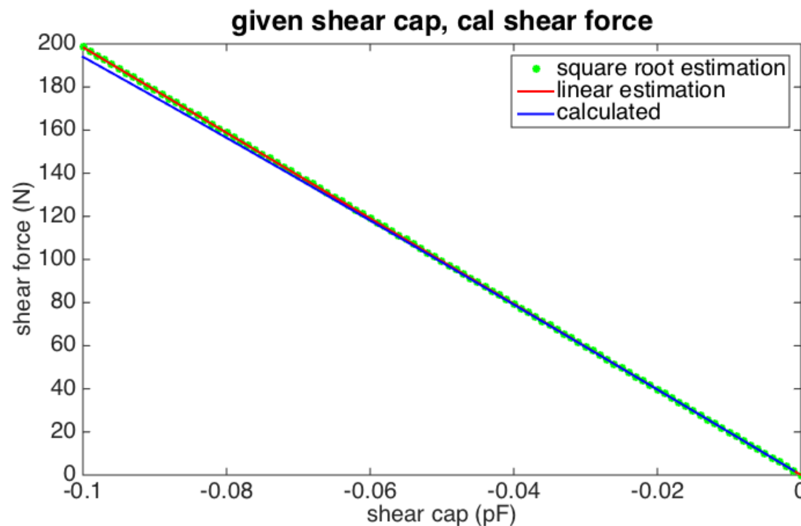

Figure 26 Square-root estimation, linear estimation, and the calculated shear force given shear capacitance

c. Considering we have coupled normal and shear force

Use square root estimation

$$F_{shear} = -\frac{\epsilon AES^2 l}{16(1+\upsilon)d^2 C_{shear}}$$

$$C_{coupled} = -\frac{\epsilon AES^2 l}{16(1+\upsilon)d'^2 F_s}$$

where we have the compressed distance between plates being:

$$d' = (1-\frac{F_N}{AE})d$$

$$C_{coupled} = -\frac{\epsilon AES^2 l}{16(1+\upsilon)(1-\frac{F_{normal}}{AE})^2 d^2 F_{shear}}$$

As long as $F_N << AE$ (180N), we can ignore the normal force to calculate the shear force.

3.4.3. Fabrication process

The fabrication process is shown step by step in Fig. 27: we start with a silicon substrate, after thermal oxidation, we get 850-nm silicon dioxide. Then we evaporate 20-nm Ti and then 300-nm Au on top before we do the liftoff process. With STS Advanced Oxide Etcher (AOE) which is capable of deep etching (>50 microns) of oxide with high selectivity to resist and silicon, we can selectively remove the backside silicon dioxide. It is followed by a 300-micrometer Plasma-Therm deep silicon etch. Next, we can spin on and then cure the PDMS, with the curing agent to PDMS at 1:5 ratio. We repeat the evaporation and liftoff process with 20-nm Ti and 300-nm Au to get the top seven pads as electrodes. Finally, we can cleave the sample to get the device.

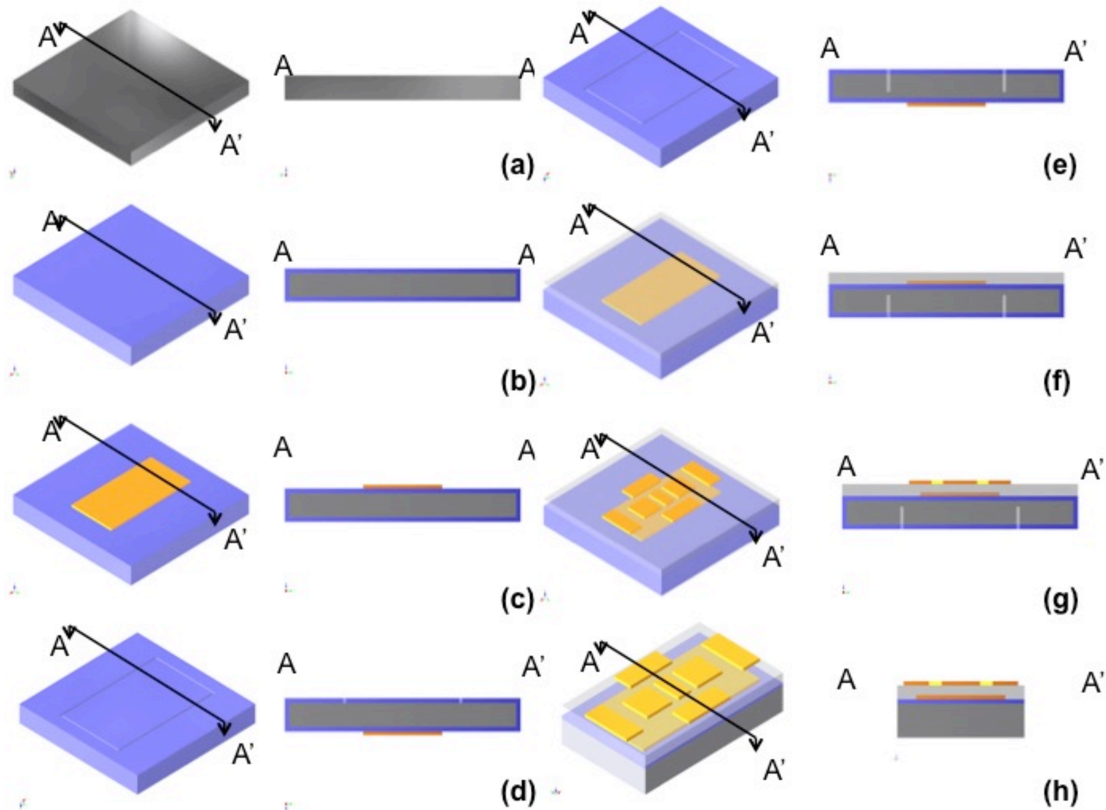

Figure 27 Fabrication process (a) silicon substrate (b) thermal oxidation 850nm (c) evaporation and liftoff (d) selective removal of backside silicon dioxide (e) 300um deep FDRIE (f) spin on and cure PDMS (g) evaporation and liftoff (h) cleave sample and release final device

3. 5 Discussion

So far, we have designed three capacitive sensor models, the comb drive model, the joystick model and the single-sided model to be integrated with robotic grasper in surgery. All three designs are based on differential capacitive measurement for the benefit of tilt compensation and temperature, humidity, and pressure variance tolerance.

References

[1] Cheng, Ming-Yuan; Lin, Chun-Liang; Lai, Yu-Tse; Yang, Yao-Joe. 2010 "A Polymer-Based Capacitive Sensing Array for Normal and Shear Force Measurement." *Sensors* 10, no. 11: 10211-10225.

[2] Dobrzynska J.A., & Gijs M.A.M. 2013 "Polymer-based flexible capacitive sensor for three-axial force measurements," *J. Micromech. Microeng*. 23 015009 doi: 10.1088/0960 -1317/23/1/015009

[3] Surapaneni R. et al 2013 "A three-axis high-resolution capacitive tactile imager system based on floating comb electrodes," *J. Micromech. Microeng*. 23 075004 doi:10.1088/0960-1317/23/7/075004

[4] Brookhuis, R.A., Droogendijk, H., Boer, M.J. de, Sanders, R.G.P., Lammerink, T.S.J., Wiegerink, R.J., and Krijnen, G.J.M., 2014 "Six-axis force-torque sensor with a large range for biomechanical applications," *J. Micromech. Microeng*. 24 (3). pp. 1-10. ISSN 0960-1317

[5] Analog Devices, "24-Bit Capacitance-to-Digital Converter with Temperature Sensor," AD7745/AD7746 datasheet, 2005.

Chapter 4: INTEGRATION

4.1. Integration with Operating Grasper

A paper relevant to this research regarding integration was published by Kim *et al* [1] but required modification of the tool used for surgery. Without any alternation of the surgical grasper, Fig. 28 demonstrates the basic idea of integrating the capacitive sensor to the grasper tip. The complexity of the circuit can be effectively reduced by implementing the sensor with the flexible printed circuit board (FPCB), and thus makes the device highly manufacturable.

The Capacitance-to-digital Converter (CDC) Chip AD 7746 shown in the figure offers us a simple solution to the capacitance measuring circuit, which has a resolution down to 4aF and can take in differential inputs for the two of the shear force directions. By flip-chip bonding the sensor to FPCB and integrating the CDC chip on the FPCB, we can integrate the 3-axis capacitive sensor with operating grasper. Afterwards, the capacitive data from the chip will be relayed to the microcontroller for software processing using an *I2C* interface.

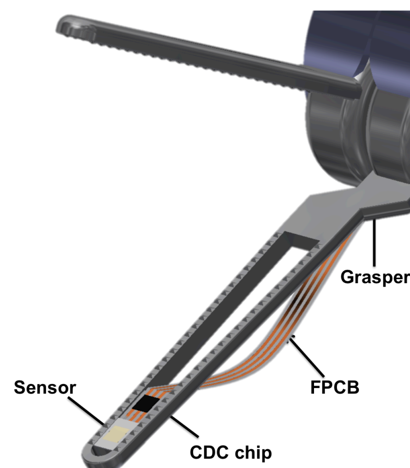

Figure 28 Schematic of integration the capacitive sensor to the surgical grasper

4.2. Capacitance-to-Digital Converter AD7746

The analog device, capacitance-to-digital converter (CDC) chip AD7746 offers us a simple solution to the capacitance measuring circuit. The AD7746 has 24-bit accuracy on capacitive data readings, and a resolution down to 4aF. It is designed for floating capacitors and can take in differential inputs for our two-direction shear force. With the help of the embedded excitation source, which can produce a 32 kHz square wave, one trace from our sensor will be connected to the excitation signal and other will be connected to the *Cin* input of the CDC.

4.2.1. Comparison between different CDCs

The reason for choosing AD7746 for our project is briefly mentioned above. Basically, the channel number, the ability to handle differential capacitance input, resolution and noise resistance capability are vital to our design. Table 6 shows a comparison between different CDCs.

The AD714x series are ideal for multiple capacitance inputs, such as a capacitor array. However, their functionality only based on single-ended sensor, we would need to utilize a differential amplifier in order to use them.

The AD774x series are based around a 24-bit sigma-delta modulator, which directly converts the capacitance value of the sensor into a 24-bit digital output. In this series, AD7745 and AD7746 are designed for floating capacitive sensors, meaning neither trace on the capacitive sensor input pins is grounded, while AD7747 is designed for grounded capacitive sensors. We chose AD7745/6 over AD7747 as AD7747 is much more prone to parasitic capacitance. Since both traces are floating in AD7745/6, only capacitance formed between the two traces will contribute to the system base capacitance.

Both AD7745 and AD7746 are good candidates for our project. The only difference is that AD7745 allows for one channel of conversion while AD7746 allows for two, where each channel can be configured as single-ended or differential, perfect for our project. We can use the single-ended mode for normal force measurement and differential mode for shear force measurement.

Table 6 Comparison for different CDCs

	Channels	Resolution	Problem/ advantage
AD7745,7746	1-2	1fF	Floating; Differential inputs
AD7747	1	1fF	1 channel; Differential, grounded
AD715X	1-2	Low	Cheap, low power consumption
AD714X	Multiple		
AD7147, 7147	13	~8fF	Grounded
AD7142	14	1fF	Need differential amplifier
AD7143	8	1fF	Grounded, Need differential amplifier

4.2.2. Pin layout for AD7746

Figure 29 displays the pin layout of the AD7746, after [2]. Details about the pin functions are provided in the datasheet [2], but the connections for our application will be described here.

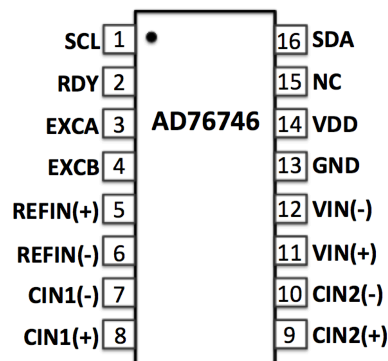

Figure 29 AD7746 pin layout

- VDD: DC voltage input. 5 V is used in our design.
- GND: Ground input.

- SCL: One-directional serial clock line. Receive information from the master device.
- SDA: Bidirectional serial data line. Transfer data bit-by-bit to and from the master device.
- EXCA/EXCB: CDC excitation signal outputs. To be routed to one trace of sensor layout, configurable 32 kHz square wave. Should be left open if not used.
- CIN1(+): CDC capacitive input in single-ended mode or one of the two capacitive channel inputs in differential operation mode. Should be left open or connect to GND if not used.
- CIN1(-): In differential operation mode, the other capacitive channel input. Connects to a separate sensor trace.

Fig. 30 gives the diagram how to connect differential capacitive sensor to AD7746. Basically, the measured capacitance is connected between the excitation source and the capacitance input *CIN(+/-)*. Then a square-wave excitation signal is applied to the measured capacitor and the modulator samples the charge going through the capacitor during the conversion time. We need to carefully choose the conversion time in order to get a desired noise performance.

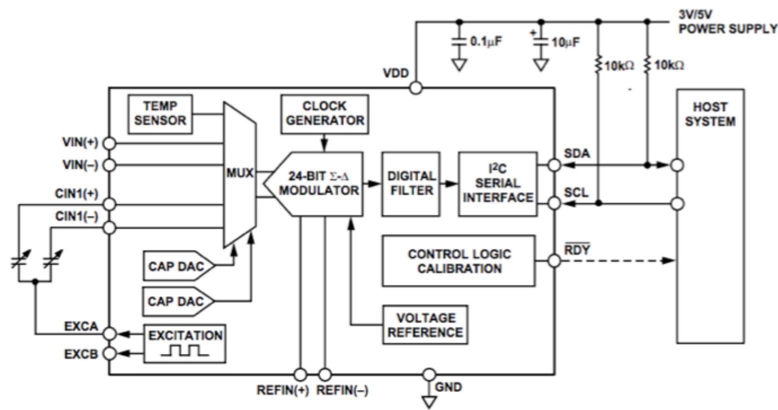

Figure 30 Application diagram for a differential capacitive sensor for chip AD7746 [2]

As for the wiring, for the joystick model, we simply need to connect the sheared bottom electrode to the excitation voltage and the top five electrodes as the capacitance inputs. While for the single-sided sensor, as displayed in Fig. 31, the left compression pad is connected to excitation pin, the right compression pad is connected to capacitance inputs to get compression capacitance; for shear force testing, the center pad is connected to excitation pin, and the surrounded four electrodes used as capacitance inputs.

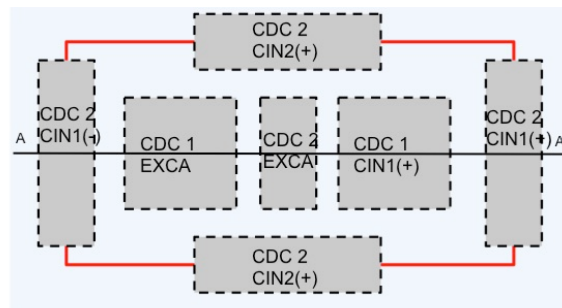

Figure 31 Illustration of wire connection for single-sided sensor with AD7746

4.2.3. Data acquisition from AD7746

Data acquisition is the process to get the real world physical property and convert it to digitalized numeric data, which can be manipulated by a computer for further analysis. In our case, the data acquisition includes, first, the capacitive sensor which can convert physical parameters into electrical signals, and next, a CDC circuit, which can convert electrical signals into a form which can be converted to digital values. It should be noted that AD7746 is not a stand-alone device, it requires a host processer (typically a microcontroller) to configure it and process the data it produces. The analysis is then performed to give us 3-axial force values as well as information about noise, resolution etc.

The interface connection mentioned above can be achieved by either employing *RS232*, USB, *I2C* (inter-integrated circuit bus), *SPI* (serial peripheral interface), *UART* (universal

asynchronous receiver transmitter) or some *GPIO* (general purpose input/output). In our case, The AD7746 supports an *I2C* compatible serial interface, thus the *I2C* interface is used.

The *I2C* communication system is a two-wire system involving a SCL (clock) and a SDA (data) line. These two wires carry all address, control, and data information bit-by-bit over the bus to and from all connected devices. The controlling processor (typically a microcontroller) in a system is known as the I2C Master, and the devices under control, are known as the *I2C* Slaves (AD7746). The Master is responsible for producing the clock signal that synchronizes the Master and Slave devices, and for initiating all data communications between the two devices using standardized procedures as shown below:

1. Data Transfer is initiated with a START bit signaled by SDA being pulled low while SCL stays high.
2. SDA sets the first data bit level while keeping SCL low.
3. The data is received when SCL rises for the first bit.
4. This process repeats, SDA transits while SCL is low, and the data is read while SCL is high.
5. A STOP bit is signaled when SDA is pulled high while SCL is high.

The Slave AD7746 measures the capacitance and converts it to digital data which is stored in three 8-bit registers inside AD7746. This data is passed onto the register block through the I2C bus, which can be then processed and analyzed by the microcontroller.

There are a total of 19 registers in AD7746. The 10 registers of interest to our project are status register, capacitance data register H, capacitance data register M, capacitance data register L, configuration register, cap DAC A and capacitance setup register.

- Status register: provides details on the current status of the AD7746 converter to the Master.
- Cap data High/ Med/ Low register: three separate registers containing the current capacitive data from the capacitive sensor.
- Cap setup register: allows configuration of the capacitance input.
- Volt setup register: allows configuration of the voltage input.
- Excitation setup register: allows configuration of the excitation signals.
- Configuration register: allows configuration of the mode of operation of the AD7746.
- Cap DAC A/B register: stores the capacitance data used to null out the base capacitance for channel 1/ channel 2.

The first four registers are read-only registers while the next six are read/write registers and they need to be set initially for a particular value before the capacitance measurement. Table 7 shows the condition for the above-mentioned 10 registers under several different situations.

Table 7 Register condition for different situations

Register	Address Pointer (Hex)	Direction Read (R) Write (W)	No Sensor Connection	Connect Sensor	CH1, EXCA, Single-ended, Continuous
Status	0x00	R	FF	7	2
Cap Data H	0x01	R	FF	0	80
Cap Data M	0x02	R	FF	0	19
Cap Data L	0x03	R	FF	0	6C
Cap Setup	0x07	R/W	FF	0	80
VT Setup	0x08	R/W	FF	0	1
EXC Setup	0x09	R/W	FF	3	B
Configuration	0x0A	R/W	FF	A0	A1
Cap DAC A	0x0B	R/W	FF	0	0
Cap DAC B	0x0C	R/W	FF	0	0

To understand the values of the register condition, the configurations used for our operation are depicted in Table 8.

Table 8 Register configuration for proper setup

address	Register/ Bit default value	7	6	5	4	3	2	1	0
0x07	Cap setup register	1	0	0	0	0	0	0	0
		Enable continuous conversion		Differential mode off	Must be 0 for proper operation				
0x08	Volt setup register	1	0	0	0	0	0	0	1
		Enable V/T continuous conversion	Select internal temperature sensor			for proper opera tion			
0x09	EXC setup register	1	0	0	1	1	0	1	1
		For faster conversion time		Disable EXCB pin as excitation output		Enable EXCA pin		Set EXC voltage	
0x10	Configure register	0	0	0	1	0	0	0	1
		V/T channel conversion time 20.1 ms		Capacitive conversion time 20 ms			Continuous conversion mode		

After the initial configuration of registers of AD7746, the process of capacitance measurement followed by capacitance-to-digital conversion takes place. The digital cap data obtained is stored

in 3 registers (capacitance data register H, capacitance data register M and capacitance data register L) of *8-bit* size each, located at register pointer address *0x01, 0x02, and 0x03*, forming a *24-bit* capacitance data. The registers should be transferred and read sequentially by *I2C* bus onto our register block module.

4.3. Flexible PCB Design

4.3.1. First generation PCB design for joystick model

The printed circuit board (PCB) layout is required to integrate the sensor with a flexible PCB. We used the software Altium to create the board. First, a part for the capacitance to digital converter (AD7746) as well as the proposed capacitive sensor needs to be created.

Creating a part has three steps, defining a symbol— draw a schematic for the part; defining a package— draw the footprint for the part; and finally, defining a device— linking the footprint to the schematic. Given the footprint of AD7746 (Fig. 32a), we can make the schematic (Fig. 32b) as well as the footprint (Fig. 32c). As for the footprint, the yellow line denotes the top overlay, red denotes the top layer, and purple denotes the top solder. The device for the AD7746 chip can be used to create the schematic layout after linking the two libraries.

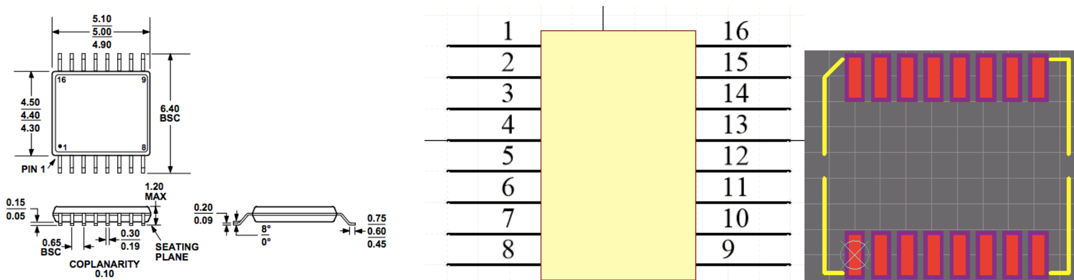

Figure 32 (a) Footprint of AD7746 (b) schematic of AD7746 (c) package of AD7746

The pin layout for AD7746 is easy to understand, Pin 1 SCL (serial clock line), Pin 2 RDY (ready), Pin 3 EXCA (excitation source A), Pin 4 EXCB (excitation source B), ignoring reference input voltage pin at Pin 5 and 6, we have Pin 7 for CIN1(-) and Pin 8 for CIN1(+). If we are considering normal force experiment only, we only need Pin 13 for GND, Pin 14 for VDD and Pin 16 for SDA (serial data line). However, if we need to test the shear force, we will still need Pin 9 for CIN2(+) and Pin 10 for CIN2(-) as channel 2 for the differential measurement.

The final schematic for the integrated circuit for the joystick model is shown in Fig. 33. Where $V_{DD}= 3V$ ($2.7V$ to $3.6V$ as recommended by the manual), $C_1= 0.1uF$, $C_2= 10uF$, $R_1= R_2= R_3= R_4= 100k\Omega$.

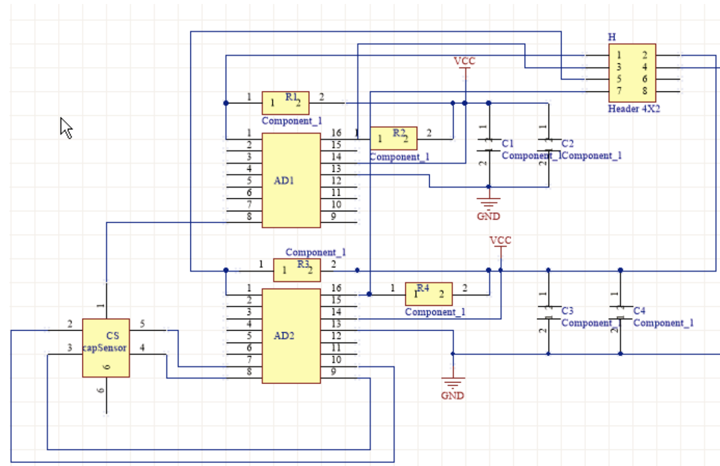

Figure 33 Schematic for joystick model integrated circuit

The general idea is demonstrated below, on the flexible PCB, the sensor is connected to two CDC chips, PC provides the CDC chips with the required DC and AC voltage while get the data from the CDC chips. Next, the LabVIEW written code communicate with the CDC chips and get the desired capacitance/ force information from the sensors.

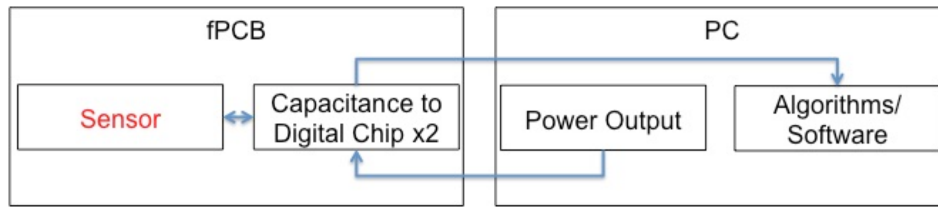

Figure 34 Working principle of the integrated capacitive sensor

In the meantime, we designed another circuit for testing the integrated circuit by replacing the capacitive sensor with two voltage-controlled capacitors (as known as varactors). We can test in parallel with sensor fabrication and validates the CDC, flexible PCB and the algorithm of the LabVIEW written code.

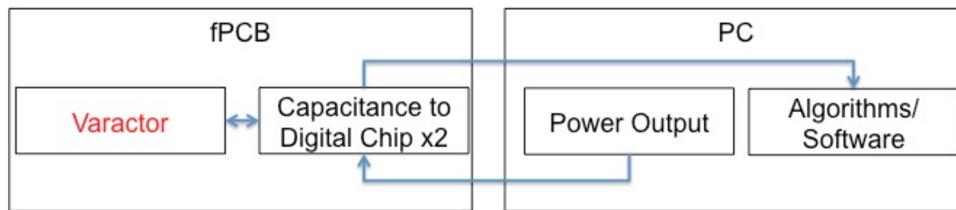

Figure 35 Working principle of the integrated voltage controlled capacitor

The validity of replacing the capacitive sensor with varactor is proven in Figure 36. (*a*) shows the force versus capacitance with our proposed capacitive sensor design while (*b*) shows the voltage versus capacitance with the chosen varactor MA46H120. Clearly, reverse biasing the varactor 4-7 volts corresponds to 250 femto-Farad to 350 femtoFarads, which is the range of our capacitive sensor. The final version for the schematic and PCB board can be seen in Fig. 37.

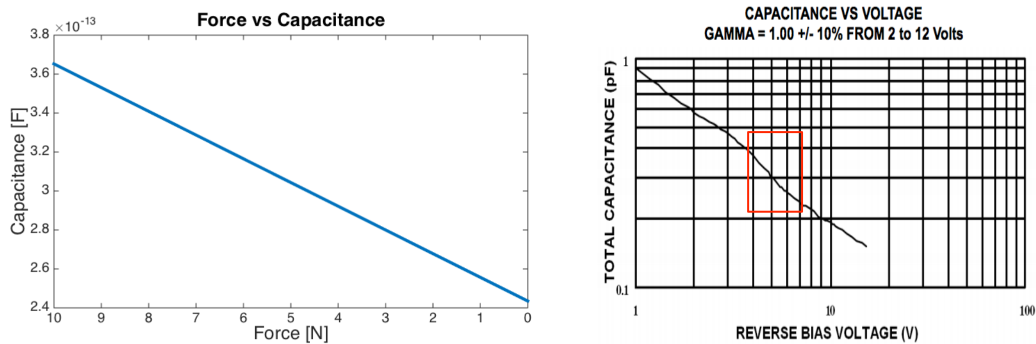

Figure 36 Comparison between capacitive sensor and varactor.

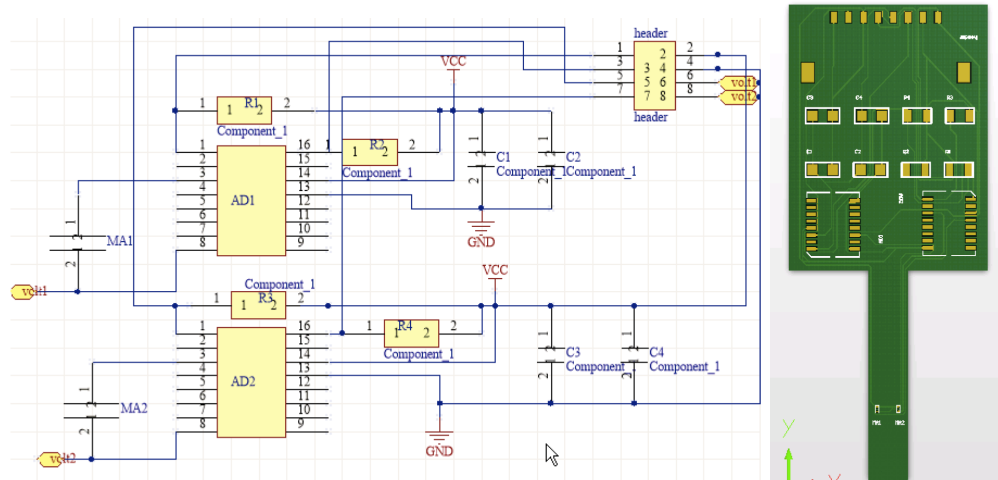

Figure 37 Schematic and 3D layout for the PCB design

4.3.2. Improved PCB design for single-sided sensor model

When turning to single-sided sensor model, the PCB design is basically the same expect for the footprint design for the sensor part. Blow shows the PCB layout and the real object (Fig. 38). In order to eliminate the interference with surgical tasks, the narrow board region is designed on purpose for grasper integration.

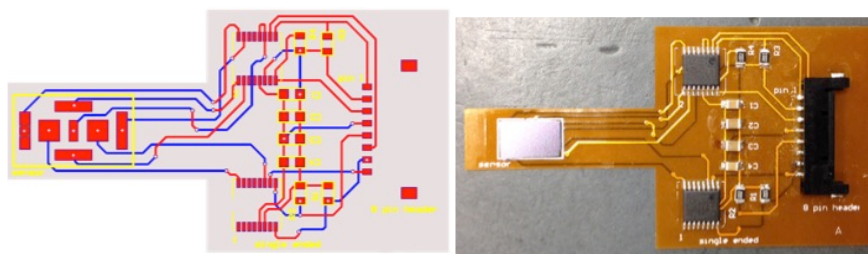

Figure 38 (left)PCB layout for single-sided sensor (right) real object after soldering components

The first improvement is to add a multiplexer. Despite the fact that AD7746 can sample capacitance with discrete frequencies up to 90 Hz it is applicable for single channel measuring only. Continuous mode with simultaneous sampling both channels is not possible by default by AD7746 since all the AD7746 chips share the same IP address. In this situation, there is no way to differentiate data from normal stress capacitance from one chip with data from shear stress

capacitance from another chip. The solution is to use a multiplexer (or MUX). A multiplexer is a device that can select one from many analog or digital inputs and forwards the selected input into a single line.

In previous design, we used two CDCs. One used 1 channel in single-ended mode for normal stress measurement and the other used 2 channels in differential mode for shear stress measurement. Now we are thinking use three CDCs with a triple 3-to-1 MUX to be treated equally. Each CDC will produce a different SDA, SCL and RDY signal. Fig. 39 shows the schematic of MUX, with *S1A/ S1B/ S1C* connecting to *x, y,* and *z* direction capacitance data inputs SDA, respectively. *S2A/S2B/S2C* connects to *x, y,* and *z* direction clock signal SCL and *S3A/S3B/S3C* connects to *x, y,* and *z* direction ready signals.

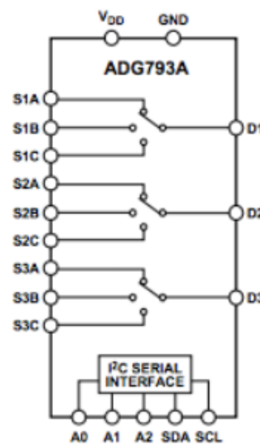

Figure 39 A triple 3-to-1 multiplexer ADG793A

Fig. 40 gives the summary of what has been done thus far: by connecting the sensor to the AD7746 capacitive to digital converter, we have information for *x, y,* and *z* direction capacitance. By using a multiplexer, we can switch between the three directions. The LabVIEW interface enables us to control whether we want to see the shear stress information or the normal stress information. What can be done next is to integrate the AD7746, the MUX, and the evaluation

board on a single FLEX and let LabVIEW to automatically switch between each channel at a high frequency, which will enable all three direction data displayed simultaneously on the screen.

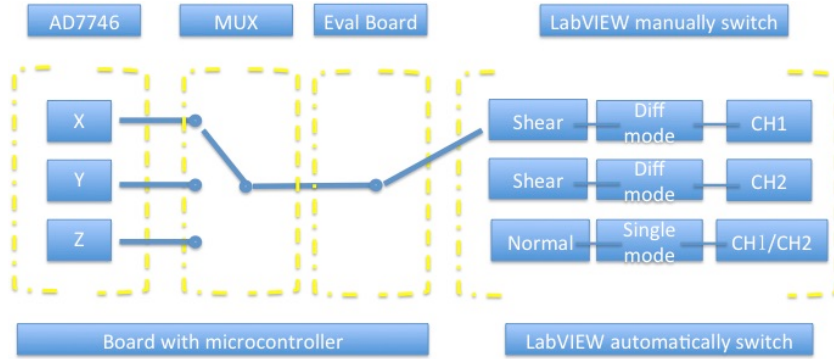

Figure 40 Schematic for now and after integration plan

Below is the schematic for the integrated FLEX board and schematic for the system level design.

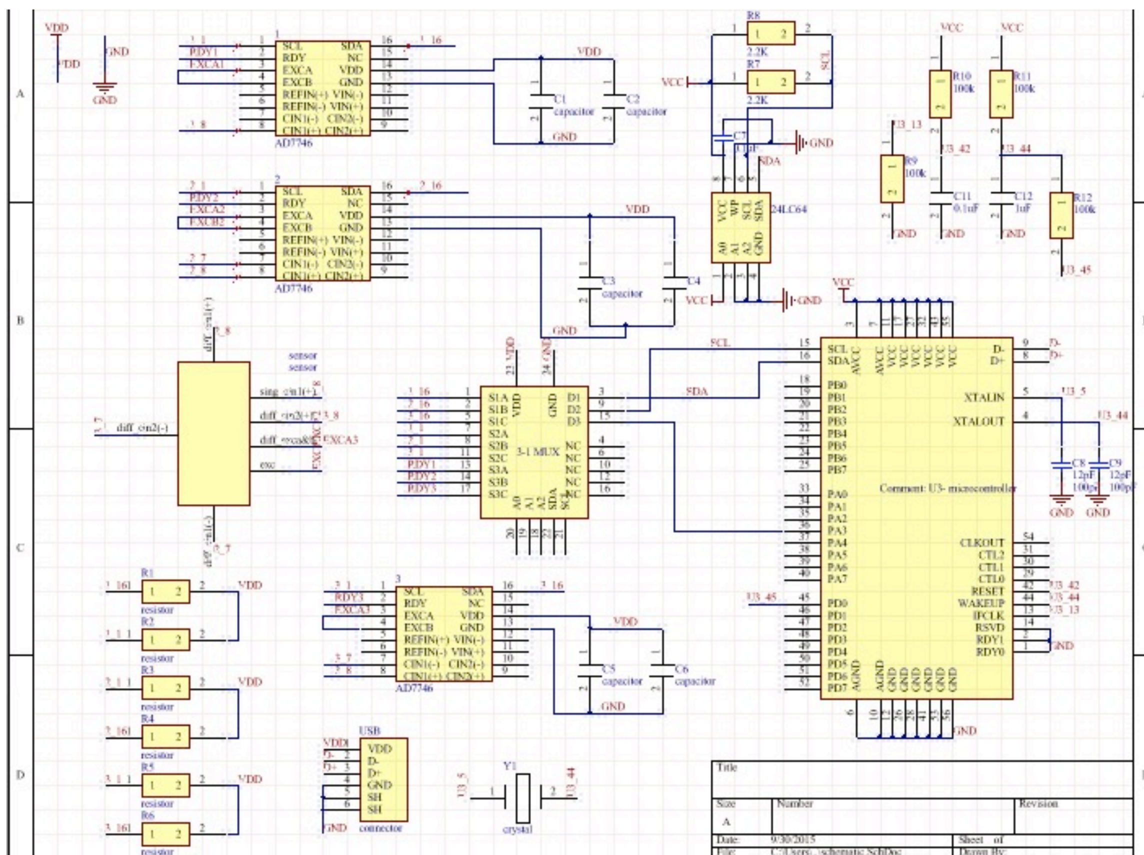

Figure 41 Screenshot for schematic for the integrated FLEX board

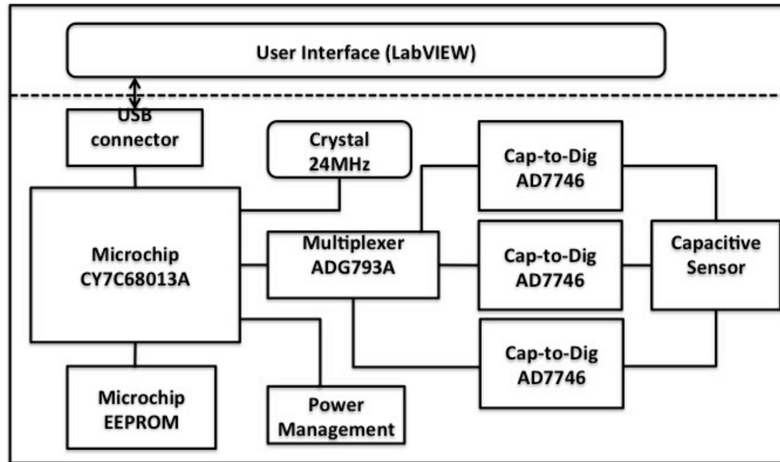

Figure 42 Schematic for system level design

4.4. Functionality Testing

This section deals with data acquisition and analysis on the collected data. Including developing an algorithm for configuring AD7746 and acquiring the stored digital capacitance data from it.

The LabVIEW code is mainly to convert the data we can obtain from the CDC chip registers to the normal and shear capacitance value we want and then convert to the normal and shear force, which is the value of interest to our collaborators, the surgeons. The first generation user interface is shown in Fig. 43, where we have three graphs each representing the normal cap code (z direction) and shear cap code (x and y direction) in hexadecimal system. On the right side, we have numbers indicating the capacitance code in hexadecimal system, in pico-Farad unit and finally, in newton system.

Figure 43 Screenshot for LabVIEW program user interface for testing AD7746

After understanding the AD7746 registers setup in previous section, below shows one example setup, which can give us continuous conversion on channel 1 with excitation source A, in differential mode with chop off at 16.1 Hz update rate with cleared CAPDAC registers. To give a little explanation, A0 in Hex for CAP setup register means 10100000 in binary for CH1 differential mode, can be used for shear *x*- direction testing. E0 in Hex for CAP setup register represents 11100000 in binary for CH2 differential mode, for shear *y*- direction testing. And 80 in Hex represents 10000000 in binary for CH1 single-ended mode, used for normal *z*- direction testing.

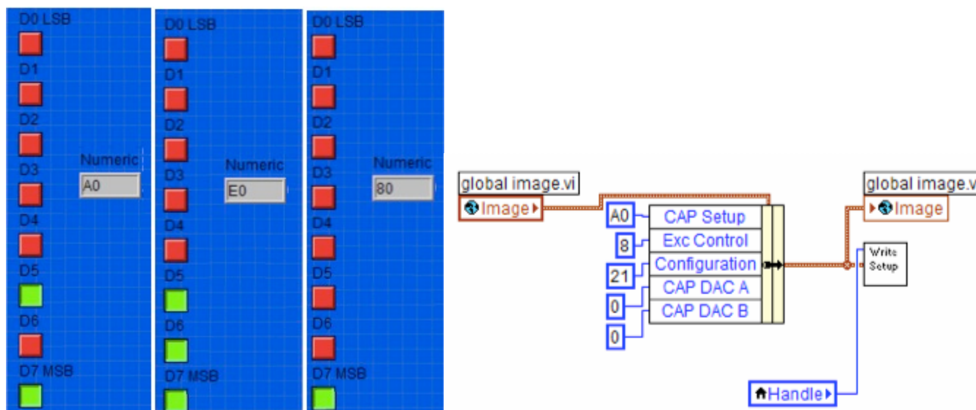

Figure 44 One example setup for the registers

The functionality of the LabVIEW software is complicated. For example, the diagram to get the capacitance and voltage data is shown in Fig. 45. The capacitance data is a *24-bit* information, from address pointer *0x01, 0x02,* and *0x03* while the voltage data is address pointer *0x04, 0x05,* and *0x06*. We need to read sequentially and change the number to boolean array, then build an array, and rebuild boolean array to number as the voltage/ capacitance value. The hexadecimal value 0x000000 represents -4.096 pF, 0x800000 represents 0 pF and 0xFFFFFF represents +4.096 pF. As a result, the conversion goes as:

$$\left(\frac{code-800000}{800000}\times Gain - offset\right)\times 4.096 \text{ pF}.$$

In order to prevent losing data, we need to wait until the conversion is complete, which requires 1 ms. Also, there are two conditions when we need to stop, one is timeout the other is when we have a register error. In the diagram, another block diagram is embedded in, which is the read register diagram.

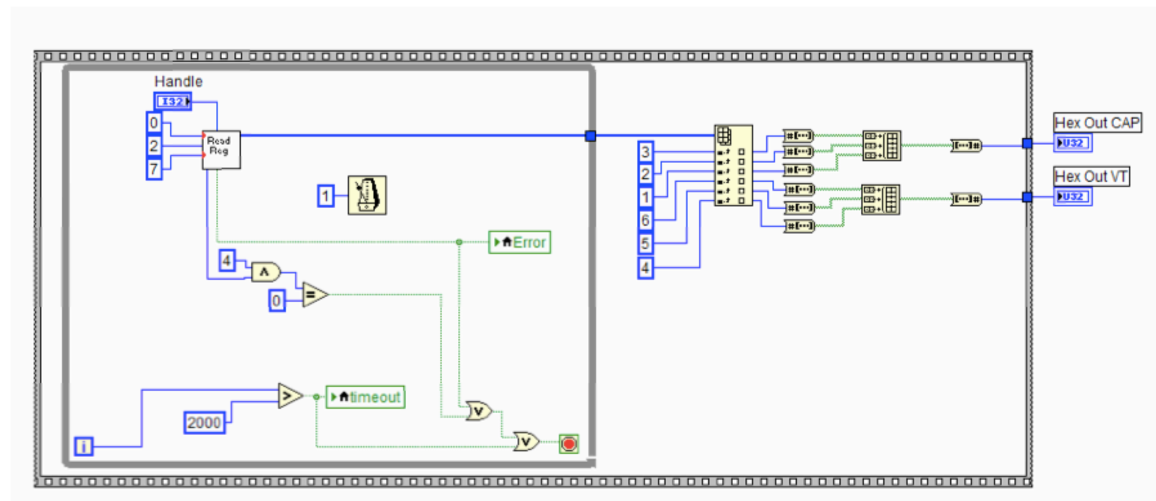

Figure 45 Screenshot for getting Hex output capacitance and voltage value diagram.

We can write to or read from all the CDC chip registers except the address pointer register, which is read only and has a total 19 address pointers, representing capacitance data, voltage data,

cap offset, cap gain, configuration, voltage setup, excitation setup etc. The address pointer register determines which register is next to perform an operation, write or read.

The read register diagram is shown blow, where we take the register address, length of the buffer and if it is 24 or 16 or 8 bit information as inputs (2 is for 24 bit, 1 for 16 bit and 0 for 8 bit) and output Hex byte 0,1,2,3. As can be seen from Fig. 46, the input value for the read register is 0, 2, and 7. Now we can understand without question that 0 is for register address, 2 is for 24 bit data retrieval, and 7 is for the buffer length. Details about the program are not included here for brevity. Just as one example, the number 90 in the graph below is caused by the reason that the start address for the CDC chip is 0x90 for a write and 0x91 for a read. Another thing worth mentioning is to reset the board before read the registers. If reset is successful, the status indication should be 7. If this is the case, we can read all other registers. Otherwise, an error light shows up and we need to set all the registers to be zero.

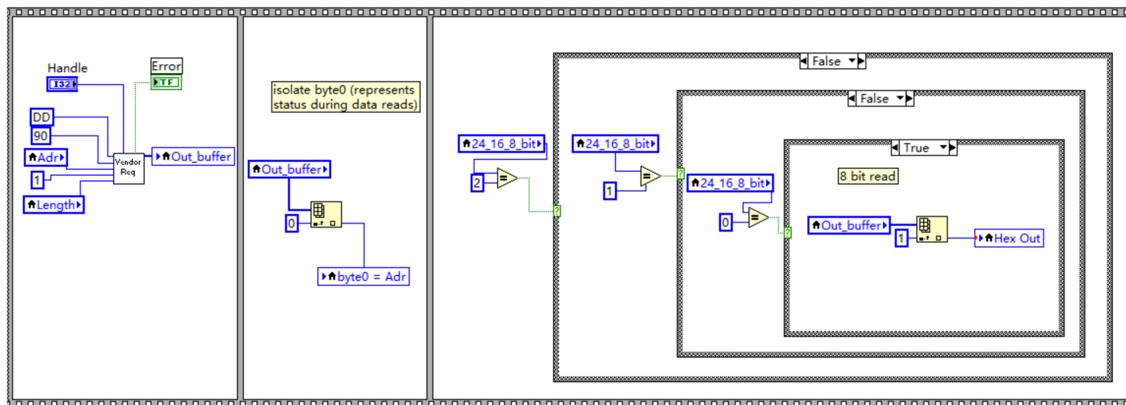

Figure 46 Screenshot for read register diagram

After getting the capacitance code, we can get the capacitance data from a simple conversion, and next, the RMS capacitance data and peak-to-peak capacitance data are known as well.

$$cap = \left(\frac{avg\ code - 800000}{800000} \times gain - offset\right) \times range\ pF$$

$$RMS\ cap = \frac{RMS\ code}{8388608} \times gain \times range\ pF$$

$$pk - pk\ cap = \frac{pk - pk\ code}{8388608} \times gain \times range\ pF$$

With this information, we are able to calculate the real-time RMS resolution and peak-to-peak resolution for the capacitive sensor, displayed in Fig. 47.

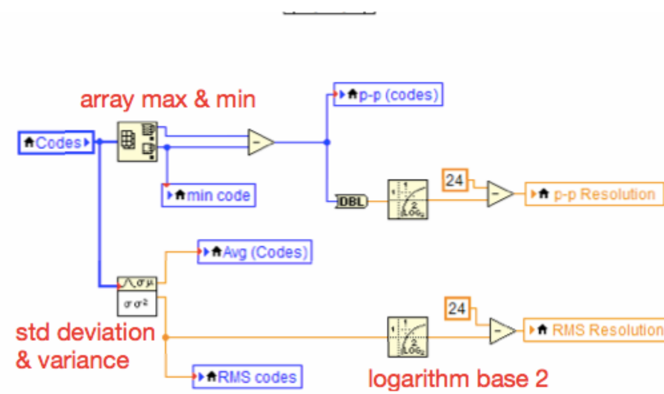

Figure 47 Screenshot for capacitance resolution calculation

In our experiment, the noise level is acquired at the beginning of the measurement to get noise analysis for a one-time testing. Then, the sensitivity value will be calculated for further real-time measurements to give us the measurement resolution. As shown in Fig. 48, after getting continuous samples, with the function of calculation unit, we can convert capacitance code to capacitance value, then, the force value can be calculated accordingly as well as the resolution, which is noise divided by sensitivity.

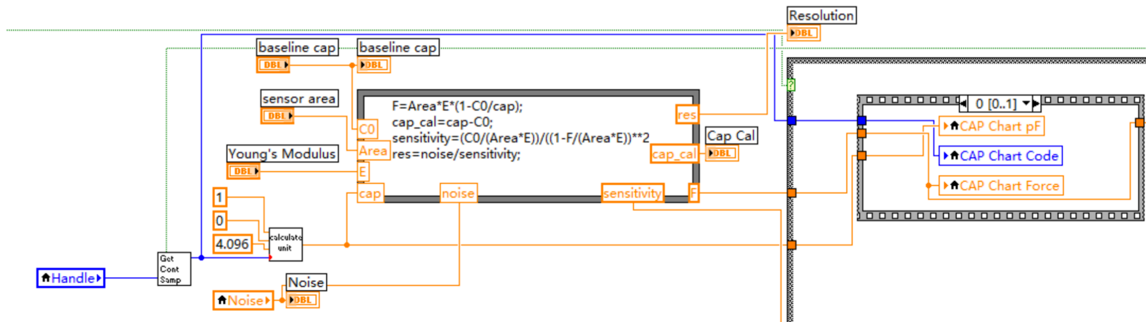

Figure 48 Screenshot for normal force calculation, sensitivity and resolution output schematic

One last improvement so far is that we added a feature for playing an alarm sound when the force exceeds 20 Newton (or whatever force value the surgeons would like).

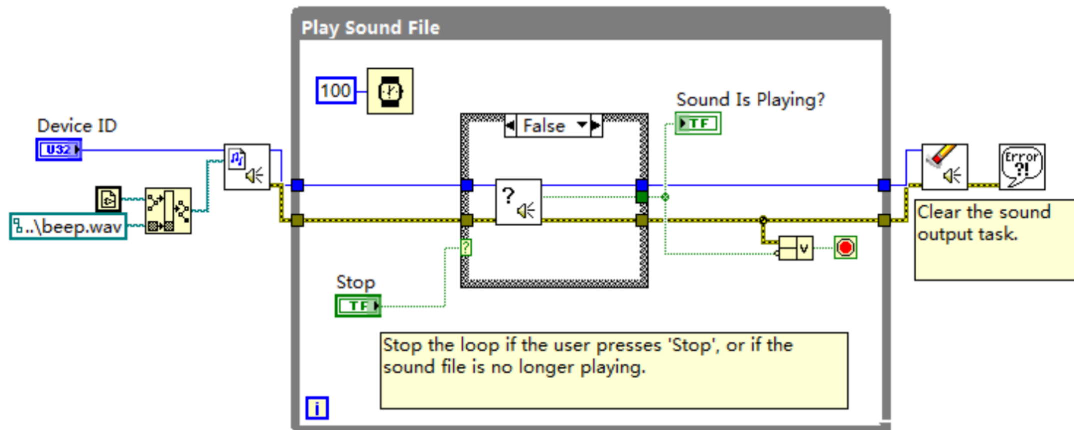

Figure 49 Play alarming sound diagram

As for commercial use/ hospital use/ testing purpose, there is no need to dig into details of the LabVIEW code. The customers will only require proper steps to use the interface. The first thing you need to do is to input sensor parameters: center plate size, side plate size, sensor area, thickness of PDMS, Young's modulus, relative permittivity, and Poisson's ratio. The parameter information is a one-time input, as long as we do not change the sensor, the values you put down will be set as default values for future usage. Then we need to setup the register for our testing, whether we use channel 1 or 2 for testing, whether it is a single-ended testing or a differential

testing, how you would you want the conversion time to be, and should it be in continuous mode or a one-time reading mode. After configured each register, we can go to the analysis tab to get the baseline capacitance and noise performance. Next, go back to the real time tab, where after hitting the start key, we can watch the capacitance, force graph as well as their values simultaneously. The data for resolution is calculated for your reference.

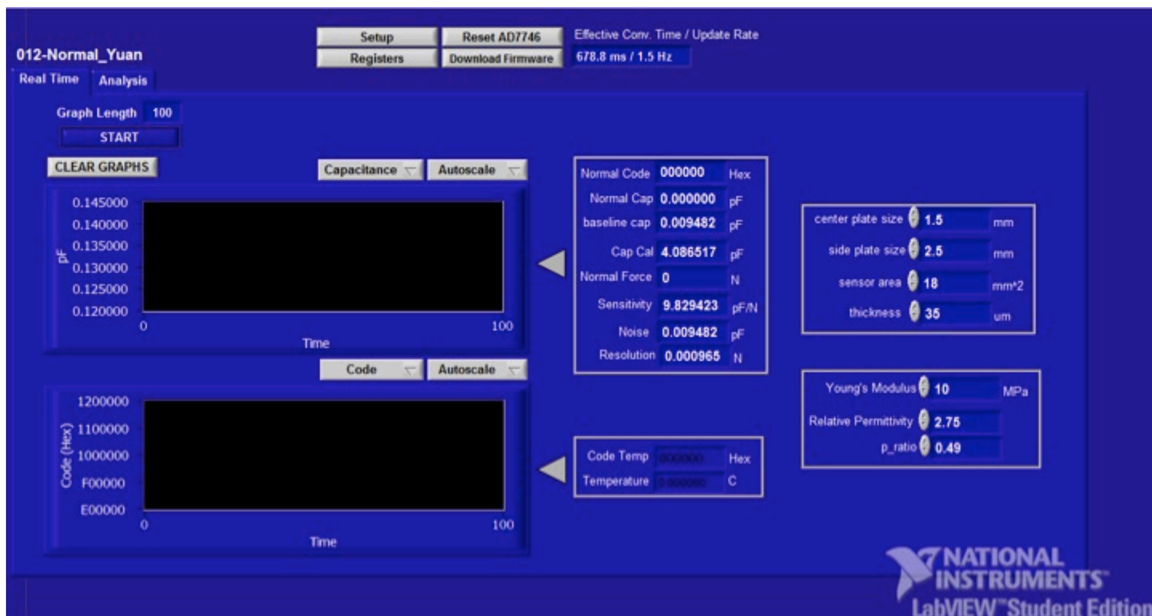

Figure 50 LabVIEW user interface

4.5. Integration with Haptic Feedback System

The current haptic feedback system (HFS) consists of a microcontroller-based printed circuits connected wirelessly, software for communication, and data processing. In order to integrate with the system, we need to adjust our system for further sensor/ actuator interfacing.

Two things need to be accommodated, the microcontroller and the software. The microcontroller used for current HFS in CASIT is AT91SAM3X8E and they use Arduino software for programming and controlling the actuators. The modification from our current system to their

system is not complicated with the help of Arduino Due.

Arduino Due is an Arduino board (shown in Fig. 51) which is based on a 32-bit microcontroller with 54 digital input/output pins, 12 analog inputs, 4 *UART*s (hardware serial ports) and a 84 MHz clock. The provided sets of digital and analog I/O pins enable interfacing to our current circuit using I2C serial communication. It also includes USB connection for loading program from personal computer to the board (see the programming port in Fig. 51). As for programming the microcontroller, the Arduino platform provides an integrated development environment (IDE) for all Arduino developers.

To make things even simpler, we can use the "Wire" library in Arduino IDE. This library allows us to communicate with our I2C device, AD7746, which have functions as begin(), requestFrom(), beginTransmission(), endTransmission(), write(), available(), read(), onReceive(), onRequest() and so on for input/output operation.

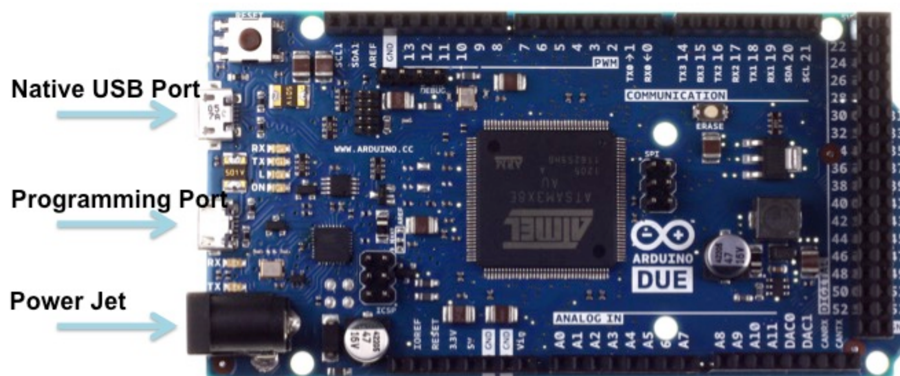

Figure 51 Arduino due board

4.6. Results and Discussion

The measurement for both normal stress testing and shear stress testing were carried out with expected results. Figure 52 shows the normal force testing with the single-sided capacitive sensor. The characterization is by applying known loads with an Instron Mechanical Loading system. The experimental data is compared with the analytical data, with acceptable discrepancy.

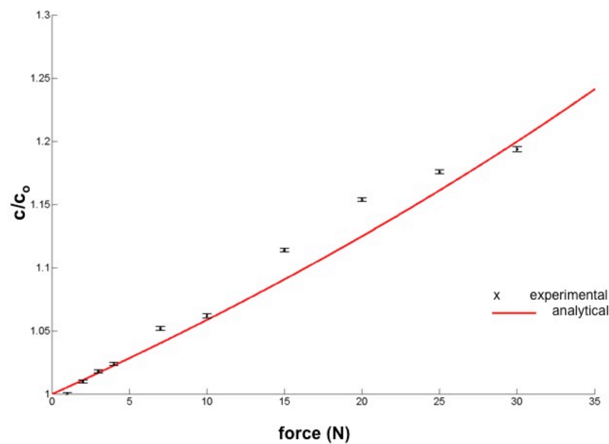

Figure 52 Normal force testing with single-sided capacitive sensor

To date, as there is no instrument available to us to apply shear force with known loads, a qualitative experiment is performed instead of a quantitative experiment and the result is shown in Fig. 53. The graph is self-explanatory as we apply a shear force towards the negative direction, we can get a increased differential capacitance value, when we apply a force towards the positive direction, we will get a decreased differential capacitance value as expected.

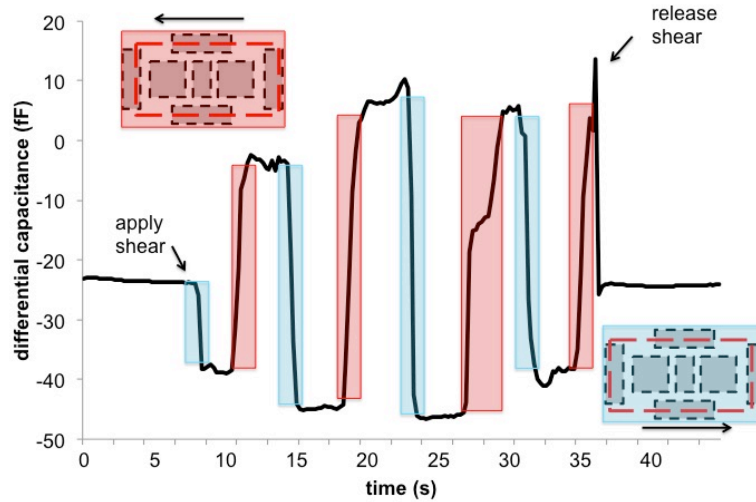

Figure 53 Shear force testing with single-sided capacitive sensor. Blue regions indicate shear displacement in the +x direction. Red regions indicate shear displacement in the –x direction. The displacement was held fixed in the space between the blue and red regions.

For the normal force testing, since the sensitivity is related to the applied force, no accurate value for the resolution (noise/ sensitivity) can be obtained. An approximation for resolution with no force applying is *20 aF/ (0.02 pF/N)= 1 mN*. For the shear force testing, the resolution value is approximately *20 aF/ (0.5 fF/N)= 4 mN*. Further measurement will be carried out with respect to getting resolution value for both normal and shear data as well as integrating with the current Haptic Feedback System. Before that, there are several possible factors that will prevent us from seeing the desired resolution.

First, the complicated circuitry embedded in AD7746 capacitance to digital converter chip will bring in noise due to the self-heating process. A temperature sensor in AD7736 helps to reveal this effect: $temperature(°C) = \frac{code}{2048} - 4096$. By tracking the temperature change and simulation in COMSOL, the self-heating induced noise can be compensated.

Second, from the datasheet, it is seen that the capacitive input noise is related to the conversion time. Shown in table 9 [2]. By taken the conversion time into consideration, and carefully chose the conversion time, we can minimize the noise and calculate the effective resolution from RMS noise.

Table 9 Typical capacitive input noise vs. conversion time

Conversion time	***Output data rate (Hz)***	***RMS noise (aF)***	***p-p noise (aF)***
11.0	90.9	40.0	212.4
11.9	83.8	27.3	137.7
20.0	50.0	12.2	82.5
38.0	26.3	7.3	50.3
62.0	16.1	5.4	33.7
77.0	13.0	4.9	28.3
92.0	10.9	4.4	27.8
109.6	9.1	4.2	27.3

Third, as mentioned in Chapter 3, the thickness of the PDMS is hard to control, while the sensitivity of the capacitive sensor is inversely proportional to the thickness. An accurate way to determine the height of PDMS is essential to the conversion of capacitance to force in the program as well as other parasitic capacitance existing in the read-out circuit.

Fourth, the cross-talk in between the top Au plates and the bottom plate brings in noise. Ways to determine and minimize this noise source is under consideration, including shielding and grounding techniques, sampling charge one plate at a time and using vias to reduce the complicity of wiring.

References

[6] Kim, U., Lee, D.H., Moon, H., Koo, J.C., Choi, H.R., "Design and realization of grasper-integrated force sensor for minimally invasive robotic surgery," *Intelligent Robots and Systems* (IROS 2014), 2014 IEEE/RSJ International Conference on, vol., no., pp.4321, 4326, 14-18 Sep, 2014

[7] Analog Devices, "24-Bit Capacitance-to-Digital Converter with Temperature Sensor," AD7745/AD7746 datasheet, 2005.

Chapter 5: SUMMARY

In this paper, we have summarized the major tactile sensor technologies used for the medical surgery, piezoresistive sensors, piezoelectric sensors, optical sensors, magnetic sensors and the one we used for our project, capacitive sensors. Each sensor modality has its own advantages and disadvantages. The reason we choose capacitive sensors is we can overcome its shortcoming of complicated circuitry and noise sensitivity by using an existing capacitive to digital conversion chip, AD7746. Three capacitive sensor models have been proposed and all analytical and simulation results are given. Comb drive model offers better sensitivity. However, we chose joystick model over comb drive model for its simpler circuit and wiring and small footprint. And the single-sided capacitive sensor model is the winner among the three for easier integration purpose. By using flexible printed circuit board to integrate the sensor with the readout circuit, we are able to evaluate our sensor system with a LabVIEW programmed user interface. The final goal of integration with the current haptic feedback system is achieved by modification of the microcontroller and the software.

For future work, we are first going to fabricate more optimized capacitive sensors for testing. Then, we can electrically characterize the fabricated sensors with LabVIEW after making our own actuator, which can apply pre-defined normal and shear stress. An additional research issue to be tackled is sterilization. The preliminary idea involves autoclave and/or chemical treatment. Finally, the integration with the HFS needs to be carried out.